

Loss Cone Dynamics

David Merritt

School of Physics and Astronomy, Rochester Institute of Technology, Rochester, New York 14623, USA

E-mail: merritt@astro.rit.edu

Abstract. Supermassive black holes can capture or disrupt stars that come sufficiently close. This article reviews the dynamical processes by which stars or stellar remnants are placed onto loss-cone orbits and the implications for feeding rates. The capture rate is well defined for spherical galaxies with nuclear relaxation times that are shorter than the galaxy's age. However, even the dense nucleus of the Milky Way may be less than one relaxation time old, and this is certainly the case for more massive galaxies; the capture rate in such galaxies is an initial-value problem with poorly-known initial conditions and the rate can be much higher, or much lower, than the rate in a collisionally relaxed nucleus. In nonspherical (axisymmetric, triaxial) galaxies, torquing of orbits by the mean field can dominate perturbations due to random encounters, leading to much higher capture rates than in the spherical geometry, particularly in (massive) galaxies with long central relaxation times. Relativistic precession plays a crucial role in mediating the capture of compact remnants from regions very near to the black hole, by destroying the orbital correlations that would otherwise dominate the torques. The complex dynamics of relativistic loss cones are not yet well enough understood for accurate estimates of compact-object ("EMRI") capture rates to be made.

1. Introduction

A supermassive black hole (SBH) at the center of a galaxy acts like a sink, removing stars that come sufficiently close to it. This removal can occur in one of two ways, depending on the mass of the SBH and on the properties of the star. At one extreme, the “star” can itself be a gravitationally compact object: a stellar-mass black hole or a neutron star. For such objects, tidal stresses from the SBH are unimportant, and removal occurs only when the object finds itself on an orbit that takes it inside the SBH event horizon. Ordinary stars can also be swallowed whole, but only if they manage to resist being pulled apart by tidal stresses from the SBH. The tidal disruption radius r_t —the distance from the SBH at which a star would be disrupted—is defined as

$$r_t = \left(\eta^2 \frac{M_\bullet}{m_\star} \right)^{1/3} R_\star \quad (1a)$$

$$\approx 1.1 \times 10^{-5} \eta^{2/3} \left(\frac{M_\bullet}{10^8 M_\odot} \right)^{1/3} \left(\frac{m_\star}{M_\odot} \right)^{-1/3} \left(\frac{R_\star}{R_\odot} \right) \text{ pc} \quad (1b)$$

where R_\star, m_\star are the radius and mass of the star and M_\bullet is the SBH mass. The quantity η^2 can be interpreted as the ratio between the duration of periapsis passage at $r_{\text{peri}} \approx r_t$ and the hydrodynamic timescale of the star, and it can be calculated given the internal properties of the star. For stars modelled as polytropes, with gaseous equations of state $P = K\rho^{(n+1)/n}$, η is related to the polytropic index n as follows [11]:

n :	3	2	1.5	1	0
η :	0.844	1.482	1.839	2.223	3.074

For the Sun, $n \approx 3$ and $\eta \approx 0.844$. Comparing r_t with the SBH gravitational radius $r_g \equiv GM_\bullet/c^2$ yields the ratio

$$\Theta \equiv \frac{r_t}{r_g} \approx 2.2 \eta^{2/3} \left(\frac{M_\bullet}{10^8 M_\odot} \right)^{-2/3} \left(\frac{m_\star}{M_\odot} \right)^{-1/3} \frac{R_\star}{R_\odot} \quad (2)$$

which implies that tidal disruption occurs outside of the SBH’s event horizon for solar-type stars when $M_\bullet \lesssim 10^8 M_\odot$. A more useful comparison is between r_t and r_c , the periapsis radius of the critical orbit that just continues inside the SBH. In the case of circular orbits around nonspinning (Schwarzschild) holes it is well known that the innermost stable radius is $6r_g$, changing to $1(9)r_g$ in the case of prograde (retrograde) orbits in the equatorial plane of a maximally spinning (Kerr) SBH. Circular orbits are not terribly likely however since capture of stars in galactic nuclei is more likely to be preceded by scattering onto a highly eccentric orbit, as discussed below. For such orbits the critical angular momentum for capture by a nonrotating SBH is $\sim 4GM_\bullet/c$; the periapsis of a Newtonian orbit with this value of L is $\sim 8r_g$, changing to $\sim 2(12)r_g$ for prograde (retrograde) orbits around maximally rotating SBHs [63]. For orbits out of the SBH symmetry plane, the critical angular momentum for capture depends on the inclination as well, returning to approximately the same value as for nonspinning holes as $\cos i \rightarrow 0$ [63]. From the condition $r_t > 8r_g$ we find that solar-type stars on eccentric

orbits are disrupted (not swallowed) if $M_{\bullet} \lesssim 1.2 \times 10^7 M_{\odot}$; disruption can occur for any $M_{\bullet} \lesssim 10^8 M_{\odot}$ if the star is on a less eccentric orbit, or for Kerr SBHs even more massive than $\sim 10^8 M_{\odot}$. Red giants or AGB (asymptotic-giant-branch) stars can also be disrupted (or at least tidally limited) by SBHs more massive than $10^8 M_{\odot}$. The relatively short lifetimes of these giant phases, plus the fact that “disruption” of a giant star may leave its structure nearly unchanged, complicates the calculation of tidal event rates in giant galaxies.

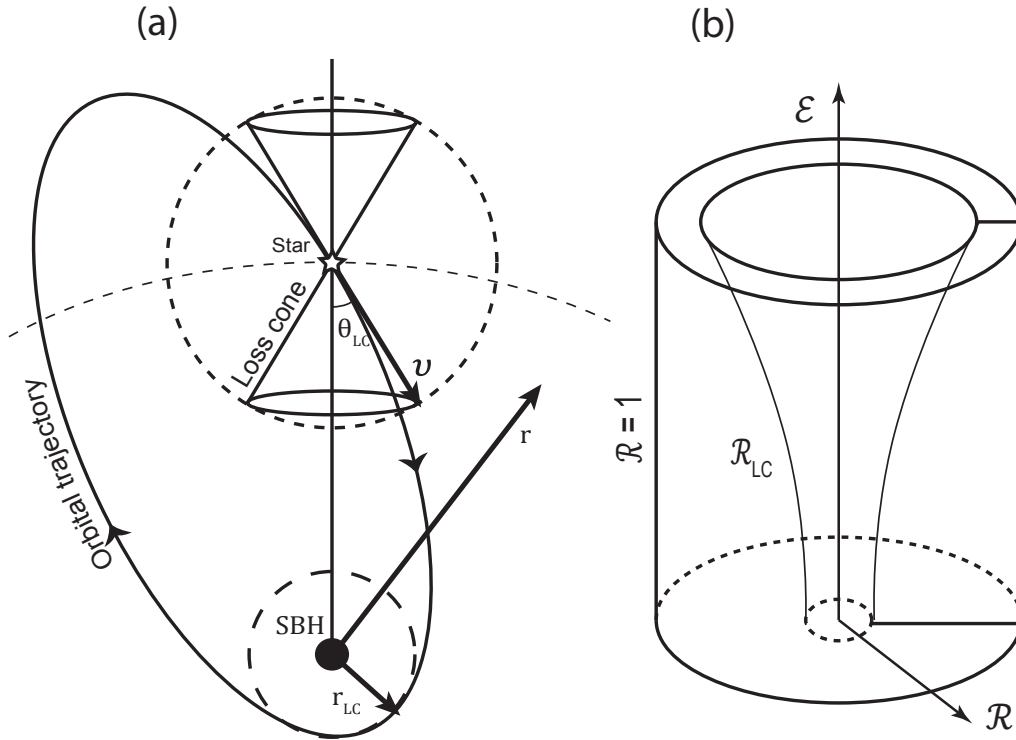


Figure 1. Two representations of the loss cone. (a) Orbits with velocity vectors that fall within the cone $\theta \leq \theta_{lc}$ will pass within the capture/disruption sphere at $r = r_{lc}$; the angle θ_{lc} is given approximately by equation (4). (b) In energy–angular-momentum space, the loss cone consists of orbits with $L \leq L_{lc}$ (equation 3). In this figure, $\mathcal{E} \equiv -E$ and $\mathcal{R} \equiv L^2/L_c(E)^2$; $\mathcal{R} = 0$ corresponds to radial orbits and $\mathcal{R} = 1$ to circular orbits. The representation of the loss cone as a cylinder is motivated by the fact that the differential equation describing SBH feeding in a spherical galaxy, equation (17), has the same form mathematically as the equation describing the flow of heat in an infinite cylinder.

The loss-cone radius r_{lc} is defined as the larger of the tidal disruption radius, r_t , or the radius of capture, r_c , for stars of a given type. An orbit that just grazes the sphere at $r = r_{lc}$ has angular momentum

$$L_{lc}^2(E) = 2r_{lc}^2 [E - \Phi(r_{lc})] \approx 2GM_{\bullet}r_{lc}; \quad (3)$$

the latter expression assumes $|E| \ll GM_{\bullet}/r_{\text{lc}}$, that is, that the star is on an orbit with semimajor axis much greater than r_{lc} . Orbits with $L \leq L_{\text{lc}}$ are called loss-cone orbits, and the ensemble of such orbits is sometimes called simply the “loss cone,” a term that derives from plasma physics [26]. The loss cone can also be visualized as the set of velocity vectors, at some distance r from the SBH, that are associated with orbits that pass within r_{lc} (figure 1a). To satisfy this condition, a star’s velocity vector must lie within a cone of half-angle θ_{lc} that is given approximately by

$$\begin{aligned} \theta_{\text{lc}} &\approx (r_{\text{lc}}/r)^{1/2}, & r \lesssim r_{\text{h}}, \\ &\approx (r_{\text{lc}}r_{\text{h}}/r^2)^{1/2}, & r \gtrsim r_{\text{h}} \end{aligned} \quad (4)$$

where

$$r_{\text{h}} \equiv \frac{GM_{\bullet}}{\sigma^2} \approx 10 \left(\frac{M_{\bullet}}{10^8 M_{\odot}} \right) \left(\frac{\sigma}{200 \text{ km s}^{-1}} \right)^{-2} \text{ pc} \quad (5)$$

is the SBH’s gravitational influence radius, defined in terms of the galaxy’s central velocity dispersion σ . (Relations 4 follow from equation 3, the first after setting $v(r) \sim \sqrt{GM_{\bullet}/r}$, the second after setting $v \sim \sigma$.) Another useful definition of “influence radius” is r_{m} , the radius containing a mass in stars equal to twice M_{\bullet} :

$$M_{\star}(r < r_{\text{m}}) = 2M_{\bullet}. \quad (6)$$

These two radii are approximately equal in galaxies with steep ($\rho \sim r^{-2}$) nuclear density profiles; for instance, in the Milky Way, $r_{\text{h}} \approx r_{\text{m}} \approx 2 - 3 \text{ pc}$.

In a spherical galaxy, the number of stars with angular momenta small enough to satisfy equation (3) would ordinarily be small; furthermore, these stars would be removed at the first periapsis passage, that is, after a single orbital period. Continued supply of stars to the SBH requires some mechanism for loss-cone repopulation: new stars need to be transferred onto loss-cone orbits, and the rate of supply of stars to the SBH will be determined by the efficiency of the resupply process. An often-discussed mechanism for loss-cone repopulation is gravitational encounters (not physical collisions) between stars, which cause their orbital elements to gradually evolve. In the case of nonspherical (axisymmetric or triaxial) nuclei, feeding rates can be high even in the absence of encounters, since fixed torques from the distributed mass will cause orbital angular momenta to change, on a timescale that is usually much less than the time associated with gravitational encounters. And even in precisely spherical nuclei, the timescale associated with gravitational encounters, the relaxation time, may be longer than the age of the Universe, which means that the distribution of orbital elements need not be anywhere near to a steady-state; in other words, loss cone repopulation may occur at a rate that depends strongly on the “initial conditions”. For all of these reasons, it is not currently possible to compute capture or disruption rates for individual galaxies with any sort of confidence.

This review focusses on the loss-cone dynamics of idealized systems: nuclei containing a single SBH, and stars, or stellar remnants, of a single mass. Readers interested in other topics related to loss cones are referred to a recent monograph [33].

2. Spherical symmetry

2.1. Basic variables and time scales

While capture or disruption occurs very near to the SBH, it turns out that the orbits that dominate the loss rate often extend much farther out, to regions where the gravitational potential $\Phi(r)$ contains contributions from the distributed mass as well as from the SBH. The appropriate orbital elements are the energy E and angular momentum L (both defined per unit mass); sufficiently close to the SBH, these can be expressed in terms of orbital semimajor axis a and eccentricity e . It is convenient to define the alternate variables

$$\mathcal{E} \equiv -E = -v^2/2 + \psi(r), \quad \mathcal{R} \equiv L^2/L_c^2(E) \quad (7)$$

where $\psi(r) = -\Phi(r) = GM_\bullet/r - \Phi_\star(r)$ and $L_c(\mathcal{E})$ is the angular momentum of a circular orbit of energy \mathcal{E} ; the scaled angular momentum \mathcal{R} has the desirable property that it lies between 0 and 1 regardless of \mathcal{E} , and near the SBH, $\mathcal{R} \approx 1 - e^2$. In terms of the angle θ_{lc} defined in figure 1, $\mathcal{R}_{lc} \equiv L_{lc}^2/L_c^2 \approx \theta_{lc}^2$. Another variable that will often be used in what follows is $\ell \equiv L/L_c = \sqrt{\mathcal{R}} \approx \sqrt{1 - e^2}$.

Once inside the loss cone, stars are lost in a time $\sim P(\mathcal{E})$, the orbital period at energy \mathcal{E} ; in the Keplerian limit,[‡]

$$P = \frac{\pi}{\sqrt{2}} \frac{GM_\bullet}{\mathcal{E}^{3/2}} = \frac{2\pi a^{3/2}}{\sqrt{GM_\bullet}} \approx 1.48 \left(\frac{M_\bullet}{4 \times 10^6 M_\odot} \right)^{-1/2} \left(\frac{a}{\text{mpc}} \right)^{3/2} \text{ yr} \quad (8)$$

(mpc \equiv milliparsecs). Repopulation via gravitational encounters occurs on a time scale that is related to the relaxation time, which for an infinite homogeneous medium is defined as [58]

$$t_r = \frac{0.34\sigma^3}{G^2 m \rho \ln \Lambda} \quad (9)$$

$$\approx 0.95 \times 10^{10} \left(\frac{\sigma}{200 \text{ km s}^{-1}} \right)^3 \left(\frac{\rho}{10^6 M_\odot \text{ pc}^{-3}} \right)^{-1} \left(\frac{m_\star}{M_\odot} \right)^{-1} \left(\frac{\ln \Lambda}{15} \right)^{-1} \text{ yr}.$$

Here ρ is the stellar density, σ is the one-dimensional velocity dispersion of the stars, m_\star is the mass of a single star, and $\ln \Lambda$, the Coulomb logarithm, is given roughly by

$$\ln \Lambda \approx \ln(M_\bullet/m_\star) \approx \ln(N_h), \quad (10)$$

with $N_h \equiv M_\bullet/m_\star$ the number of stars whose mass equals M_\bullet . For $m_\star = M_\odot$ and $M_\bullet = (0.1, 1, 10) \times 10^8 M_\odot$, $\ln \Lambda \approx (15, 18, 20)$.

In a time $\sim t_r(r_h)$, the relaxation time at the SBH influence radius, the distribution of orbital energies near the SBH will have reached a statistically “most likely” state due to gravitational encounters. The corresponding density profile, the Bahcall-Wolf cusp, turns out to follow $n(r) \propto r^{-7/4}$ at $r \lesssim 0.2r_h$ [3]. However it is not clear that the relaxation time in any nucleus with a known SBH is short enough for a Bahcall-Wolf

[‡] Non-Keplerian orbits need not be closed and may have as many as three fundamental frequencies. Here, P will always be used to refer to the radial period, i.e. the time between periapsis passages.

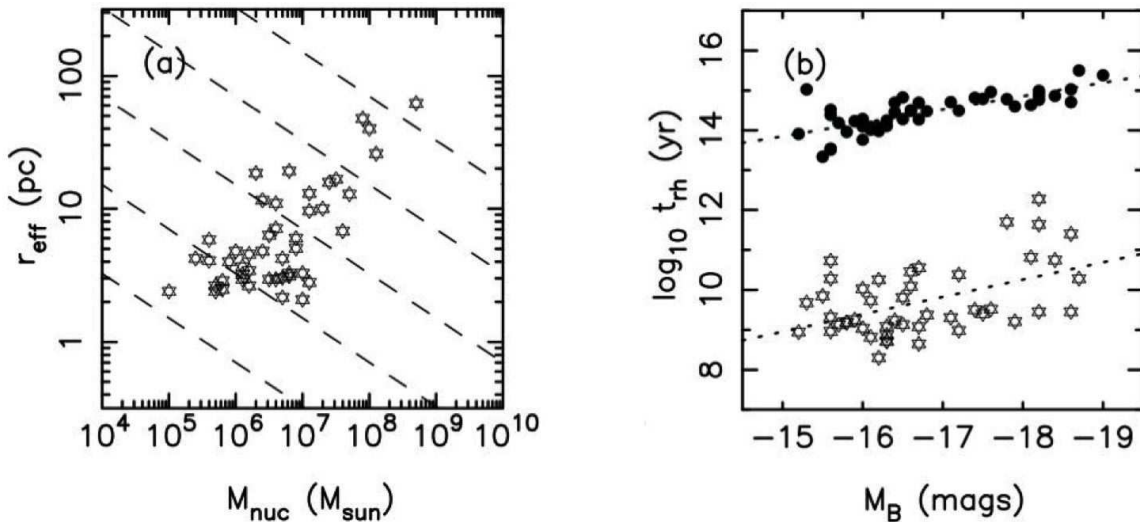


Figure 2. Properties of nuclear star clusters (NSCs) in galaxies belonging to the Virgo Galaxy Cluster [31]. The plotted points represent all Virgo galaxies, among the 100 brightest, that have compact nuclei [10]. *Left panel:* nuclear radii and masses; masses are from [55]. Dashed lines correspond to nuclear half-mass relaxation times of $(10^8, 10^9, 10^{10}, 10^{11}, 10^{12})$ years increasing up and to the right. *Right panel:* half-mass relaxation times of NSCs (\star) and their host galaxies (\bullet) plotted against absolute blue magnitude of the galaxy. Relaxation times were computed assuming $m_\star = M_\odot$. The lower dotted line is equation (11).

cusps to have formed. The Milky Way has one of the densest nuclei known, but the relaxation time at $r_h \approx 2.5$ pc is longer than 10^{10} yr [32], and careful number counts of the (old) stars inside r_h reveal a flat or declining density toward the center, not a cusp [7, 12, 4]. The galaxies most likely to contain collisionally-relaxed nuclei are those hosting so-called nuclear star clusters (NSCs), compact sub-systems with masses $\sim 0.3\%$ the total galaxy mass [15], and with half-mass (not central) relaxation times that scale approximately as

$$\log_{10}(T_{\text{rh}}/\text{yr}) \approx 9.38 - 0.434(M_B + 16) \quad (11)$$

with M_B the absolute B -magnitude of the galaxy (figure 2). These relaxation times appear to fall below 10 Gyr in galaxies with absolute magnitudes fainter than $M_B \approx -17$, or luminosities less than $\sim 4 \times 10^8 L_\odot$. The NSCs in these galaxies have masses below $\sim 10^7 M_\odot$ and half-light radii $\lesssim 10$ pc. The NSC in the Milky Way has properties that are close to these limiting values [54], consistent with the fact that its relaxation time is ~ 10 Gyr. Unfortunately no NSC beyond the Local Group is near enough that the presence of a Bahcall-Wolf cusp could be confirmed even if it were present; furthermore the typical NSC may not contain a massive black hole, although some clearly do [55].

In stellar spheroids brighter than $\sim 10^{10} L_\odot$, which typically do not contain NSCs, the relaxation time at the SBH influence radius scales approximately with SBH mass as

[36]

$$t_r(r_m) \approx 3 \times 10^{11} \left(\frac{M_\bullet}{10^7 M_\odot} \right)^{1.54} \text{ yr.} \quad (12)$$

Relaxation times in the nuclei of brighter galaxies—or equivalently, galaxies with SBH masses greater than $\sim 10^7 M_\odot$ —are probably always longer than 10 Gyr.

2.2. Steady-state loss rates

While no nucleus may be old enough for the distribution of orbital *energies* near the SBH to have reached a steady state, the distribution of orbital *angular momenta* for values near L_{lc} may nevertheless have done so, since the associated timescale is shorter by a factor $L_{\text{lc}}^2/L_c^2 \approx \mathcal{R}_{\text{lc}}^2 \ll 1$ than the energy relaxation time t_r . In fact it is common to follow a hybrid approach in the calculation of event rates, adopting whatever distribution of energies is implied by the observed $n(r)$ ($f \sim \mathcal{E}^{\gamma-3/2}$ if $n \sim r^{-\gamma}$), while the angular momentum distribution at each \mathcal{E} is assumed to have reached an approximately steady state under the influence of gravitational encounters [29].

In this approach, the equation describing the evolution of the stellar phase-space density $f(\mathcal{R}, t; \mathcal{E})$ due to gravitational encounters is the one-dimensional (angular-momentum-dependent) Fokker-Planck equation [33]:

$$\frac{\partial N}{\partial t} = -\frac{\partial}{\partial \mathcal{R}} (N \langle \Delta \mathcal{R} \rangle_t) + \frac{1}{2} \frac{\partial^2}{\partial \mathcal{R}^2} [N \langle (\Delta \mathcal{R})^2 \rangle_t]. \quad (13)$$

Here $N(\mathcal{E}, \mathcal{R}, t) d\mathcal{E} d\mathcal{R} = 4\pi^2 P(\mathcal{E}, \mathcal{R}) L_c(\mathcal{E})^2 f(\mathcal{E}, \mathcal{R}, t) d\mathcal{E} d\mathcal{R}$ is the joint distribution of orbital energies and angular momenta, and $\langle \Delta \mathcal{R} \rangle$ and $\langle (\Delta \mathcal{R})^2 \rangle$ are local, angular momentum diffusion coefficients. The subscripts t on the diffusion coefficients indicate orbit averages, for example,

$$\langle \Delta \mathcal{R} \rangle_t \equiv \frac{2}{P} \int_{r_-}^{r_+} \frac{dr}{v_r} \langle \Delta \mathcal{R} \rangle \quad (14)$$

with v_r the radial velocity along the orbit. The local diffusion coefficients can be expressed in terms of the velocity-space diffusion coefficient $\langle \Delta v_\perp^2 \rangle$; in the limit of small \mathcal{R} the relations are

$$\langle \Delta \mathcal{R} \rangle = \frac{r^2}{L_c(\mathcal{E})^2} \langle \Delta v_\perp^2 \rangle, \quad \langle (\Delta \mathcal{R})^2 \rangle = \frac{2r^2}{L_c(\mathcal{E})^2} \mathcal{R} \langle \Delta v_\perp^2 \rangle \quad (15)$$

and to lowest order in \mathcal{R} ,

$$\langle \Delta \mathcal{R} \rangle = \frac{1}{2} \frac{\partial}{\partial \mathcal{R}} \langle (\Delta \mathcal{R})^2 \rangle, \quad (16)$$

a relation that is also valid if the local diffusion coefficients are replaced by their orbit-averaged counterparts. Using (16), equation (13) can be written

$$\frac{\partial N}{\partial t} \approx \frac{1}{2} \frac{\partial}{\partial \mathcal{R}} \left[\langle (\Delta \mathcal{R})^2 \rangle_t \frac{\partial N}{\partial \mathcal{R}} \right] \approx \mathcal{D} \frac{\partial}{\partial \mathcal{R}} \left(\mathcal{R} \frac{\partial N}{\partial \mathcal{R}} \right), \quad (17)$$

where

$$\mathcal{D}(\mathcal{E}) \equiv \lim_{\mathcal{R} \rightarrow 0} \frac{\langle (\Delta \mathcal{R})^2 \rangle_t}{2\mathcal{R}} = \frac{2}{L_c^2(\mathcal{E}) P(\mathcal{E})} \int_0^{\psi^{-1}(\mathcal{E})} \frac{r^2 dr}{v_r} \langle (\Delta v_\perp)^2 \rangle \quad (18)$$

is an inverse, orbit-averaged relaxation time. Equation (17), after a trivial change of variables, has the same mathematical form as the equation governing transfer of heat in a cylindrical rod [43]. Because of this, some authors prefer the term “loss cylinder” to “loss cone,” and that is why figure 1b adopts a cylindrical geometry.

Consider steady-state solutions. Setting $N \propto \ln \mathcal{R}$ in equation (17) implies $\partial N / \partial t = 0$. As a boundary condition, it makes sense to require that N fall to zero at some finite angular momentum, say $\mathcal{R} = \mathcal{R}_{\text{lc}}(\mathcal{E})$. The steady-state solution then becomes

$$N(\mathcal{R}; \mathcal{E}) = \frac{\ln(\mathcal{R}/\mathcal{R}_{\text{lc}})}{\ln(1/\mathcal{R}_{\text{lc}}) + \mathcal{R}_{\text{lc}} - 1} \bar{N}(\mathcal{E}), \quad (19)$$

where

$$\bar{N}(\mathcal{E}) = \int_{\mathcal{R}_{\text{lc}}}^1 N(\mathcal{E}, \mathcal{R}) d\mathcal{R} \quad (20)$$

is a number-weighted average of N over angular momentum. $\bar{N}(\mathcal{E})$, and the corresponding phase-space density

$$\bar{f}(\mathcal{E}) \approx \frac{\bar{N}(\mathcal{E})}{4\pi^2 L_c^2(\mathcal{E}) P(\mathcal{E})}, \quad (21)$$

are approximately the N and f that would be inferred for an observed galaxy if it were modeled assuming an isotropic velocity distribution.

Let $F(\mathcal{E})d\mathcal{E}$ be the flux of stars (number per unit time) in energy interval $d\mathcal{E}$ centered on \mathcal{E} , into the loss cone. In general,

$$F(\mathcal{E})d\mathcal{E} = -\frac{d}{dt} \left[\int_{\mathcal{R}_{\text{lc}}}^1 N(\mathcal{E}, \mathcal{R}) d\mathcal{R} \right] d\mathcal{E}. \quad (22)$$

Substituting equation (17) into equation (22), and requiring $\partial N / \partial \mathcal{R} = 0$ at $\mathcal{R} = 1$, we find

$$F(\mathcal{E}) = \mathcal{D}(\mathcal{E}) \mathcal{R}_{\text{lc}} \left(\frac{\partial N}{\partial \mathcal{R}} \right)_{\mathcal{R}_{\text{lc}}} \approx \frac{\bar{N}(\mathcal{E}) \mathcal{D}(\mathcal{E})}{\ln(1/\mathcal{R}_{\text{lc}})}, \quad (23)$$

where the latter expression assumes $L_{\text{lc}} \ll L_c$. Equation (23) states that a fraction $\sim 1/|\ln(\mathcal{R}_{\text{lc}})|$ of stars at energies \mathcal{E} to $\mathcal{E} + d\mathcal{E}$ are scattered into the loss cone each relaxation time [19].

A subtlety arises here, since the change in a star’s angular momentum over one orbital period, δL , can be comparable to L_{lc} [28]. If this is the case, the separation of time scales on which equation (13) is based breaks down. We can parametrize the goodness of the diffusive approximation in terms of $q(\mathcal{E}) \approx (\delta L / L_{\text{lc}})^2$. Since $\delta L \approx (P/t_r)^{1/2} L_c$ and $t_r \approx \mathcal{D}^{-1}$, we can define q as

$$q(\mathcal{E}) \equiv \frac{P(\mathcal{E}) \mathcal{D}(\mathcal{E})}{\mathcal{R}_{\text{lc}}(\mathcal{E})} \quad (24)$$

where $P(\mathcal{E}) \equiv P(\mathcal{E}, \mathcal{R})_{\mathcal{R} \rightarrow 0}$. Near the SBH, orbital periods are short, and stars hardly penetrate beyond the loss-cone boundary before they are consumed or destroyed. At these energies, $q \ll 1$ and the phase-space density vanishes throughout the loss cone

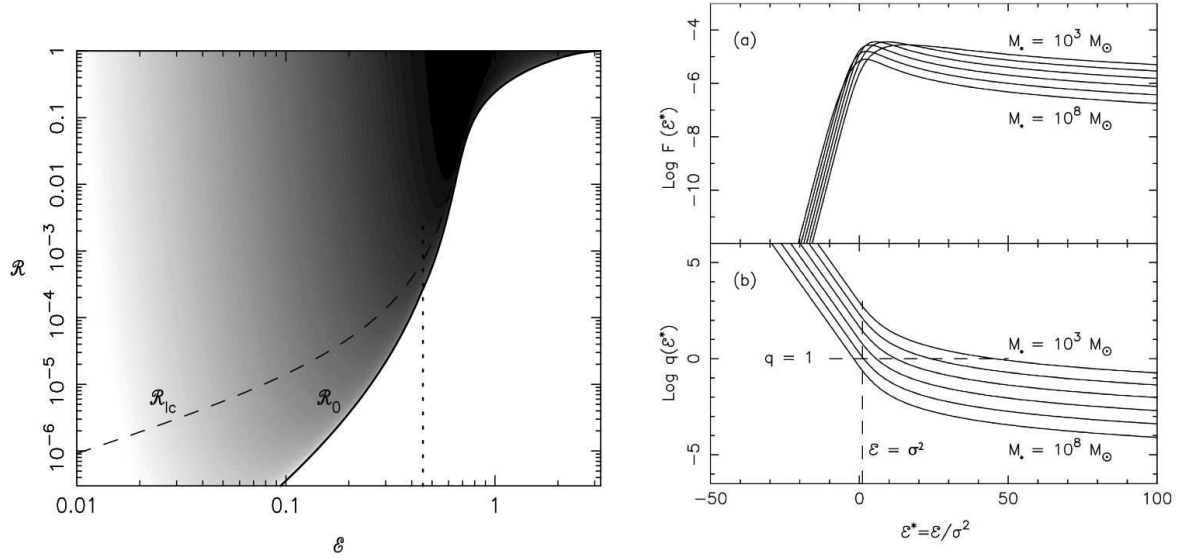


Figure 3. *Left:* the Cohn–Kulsrud steady-state solution for $f(\mathcal{R})$. The gray scale is proportional to the logarithm of f . \mathcal{R}_{lc} is the dimensionless angular momentum of an orbit that grazes the loss sphere. The vertical dotted line marks the energy at which $q = 1$; to the left, $q \gg 1$ and $\mathcal{R}_{lc} \gg \mathcal{R}_0$ (full loss cone); to the right, $q \ll 1$ and $\mathcal{R}_{lc} \ll \mathcal{R}_0$ (empty loss cone). *Right:* (a) Energy-dependent flux of stars into the loss cone of an SBH embedded in an “isothermal” nucleus, with density and potential given by equation (31) [62]. Solar-type stars were assumed, and the M_\bullet – σ relation was used to relate σ to M_\bullet . (b) The dimensionless function $q(\mathcal{E})$ that describes the degree to which the loss cone is filled by gravitational scattering. For small M_\bullet , most of the stars inside the SBH influence sphere are in the full-loss-cone regime.

except for a very small region near the boundary—this is the empty-loss-cone, or diffusive, regime. For small \mathcal{E} , on the other hand, P is large and \mathcal{R}_{lc} is small; at these energies it is possible for a star to diffuse across the loss cone by gravitational encounters during a *single* orbital period. Consider an orbit inside the loss cone. At $r = r_{lc}$ on such an orbit, there are no stars moving in an outward direction; but if one were to follow the orbit outward, stars from neighboring orbits would be scattered onto it. This argument suggests that, for $q \gg 1$, even orbits inside the loss cone will be fully populated—this is the full-loss-cone, or pinhole, regime.

In terms of q , the flux in the diffusive regime (23) is

$$F^{\text{elc}}(\mathcal{E}) \approx \frac{q}{\ln(1/\mathcal{R}_{lc})} \frac{\bar{N}\mathcal{R}_{lc}}{P}, \quad q \ll 1 \quad (25)$$

while in the pinhole regime, stars are supplied to the SBH at the same rate as if they simply followed their unperturbed orbits:

$$F^{\text{flc}}(\mathcal{E}) \approx \frac{\bar{N}\mathcal{R}_{lc}^2}{P}, \quad q \gg 1 \quad (26)$$

independent of the rate of encounters.

It turns out that the flux of stars into the SBH can contain substantial contributions both from the diffusive and pinhole regimes. This fact necessitates a quantitative

understanding of how stars get into the loss cone even at energies where the orbit-averaged approximation breaks down. By returning to the local (radius-dependent) Fokker-Planck equation, Cohn & Kulsrud [9] found that the density near the loss cone could be expressed approximately in terms of an equation like (19):

$$N(\mathcal{R}; \mathcal{E}) = \frac{\ln(\mathcal{R}/\mathcal{R}_0)}{\ln(1/\mathcal{R}_0) + \mathcal{R}_0 - 1} \bar{N}(\mathcal{E}), \quad (27)$$

where $\mathcal{R}_0 = \mathcal{R}_0(\mathcal{E}) = \mathcal{R}_0[q(\mathcal{E})]$ is given by [33]

$$\mathcal{R}_0(q) = \mathcal{R}_{\text{lc}} e^{-q/\xi(q)}, \quad \xi(q) \equiv 1 - 4 \sum_{m=1}^{\infty} \frac{e^{-\alpha_m^2 q/4}}{\alpha_m^2} \quad (28)$$

and the α_m are consecutive zeros of the Bessel function $J_0(\alpha)$. For small q , $\xi \approx (2/\sqrt{\pi})\sqrt{q} \approx 1.13\sqrt{q}$; a good approximation for arbitrary q is $\xi \approx (q^2 + q^4)^{1/4}$. In the Cohn–Kulsrud solution, the phase-space density falls approximately to zero, not at \mathcal{R}_{lc} , but at a smaller angular momentum \mathcal{R}_0 , and the separation between \mathcal{R}_{lc} and \mathcal{R}_0 increases as one moves farther from the SBH, i.e. to lower \mathcal{E} . The left panel of figure 3 illustrates the full solution; the transition from empty- to full-loss-cone regimes takes place at $\mathcal{E} \approx \mathcal{E}_{\text{crit}}$ where $q(\mathcal{E}_{\text{crit}}) = |\ln \mathcal{R}_{\text{lc}}(\mathcal{E})|$. The loss-cone flux in the Cohn–Kulsrud solution (number of stars per unit time per unit energy) can be expressed in terms of the full-loss-cone flux defined in equation (26) as

$$F(\mathcal{E}) \approx q(\mathcal{E}) \frac{F^{\text{flc}}(\mathcal{E})}{\ln(1/\mathcal{R}_0)} \quad (29)$$

which, in the large- q and small- q limits, has the expected forms

$$F/F^{\text{flc}} \approx q |\ln \mathcal{R}_{\text{lc}}|^{-1}, \quad q \ll -\ln \mathcal{R}_{\text{lc}} \quad (30a)$$

$$\approx 1, \quad q \gg -\ln \mathcal{R}_{\text{lc}}. \quad (30b)$$

Given the Cohn–Kulsrud solution for $f(\mathcal{R})$, the loss rate can be computed for any $\{M_{\bullet}, n(r), m_{\star}, r_{\text{lc}}\}$ using (24-29). A concrete nuclear model, and one that describes the NSCs of the Milky Way and some other Local Group galaxies (M32, NGC 205) fairly well, is the singular isothermal sphere:

$$\rho(r) = m_{\star} n(r) = \frac{\sigma^2}{2\pi G r^2}, \quad \psi(r) = \frac{GM_{\bullet}}{r} - 2\sigma^2 \ln\left(\frac{r}{r_{\text{h}}}\right). \quad (31)$$

The name derives from the fact that—in the absence of a central point mass—the velocity dispersion is independent of position and equal to the parameter σ . If we are bold enough to assume that σ is related to M_{\bullet} via the M_{\bullet} – σ relation [17], then σ , $n(r)$ and $r_{\text{h}} = GM_{\bullet}/\sigma^2$ are all determined by the single parameter M_{\bullet} . Setting $r_{\text{lc}} = r_t$ (rather than r_c) is appropriate for the low-mass SBHs that co-exist with NSCs; using equation (1), the tidal disruption radius can be written

$$\frac{r_t}{r_{\text{h}}} \approx 1.5 \times 10^{-6} \left(\frac{\eta}{0.844}\right)^{2/3} \left(\frac{\sigma}{100 \text{ km s}^{-1}}\right)^{-1.24} \left(\frac{m_{\star}}{M_{\odot}}\right)^{-1/3} \left(\frac{R_{\star}}{R_{\odot}}\right). \quad (32)$$

The right panel of figure 3 plots $F(\mathcal{E})$ and $q(\mathcal{E})$ in isothermal nuclei for various values of M_{\bullet} , assuming $m_{\star} = M_{\odot}$ and $R_{\star} = R_{\odot}$. The flux exhibits a mild maximum at $\mathcal{E} \approx \sigma^2$

and falls off slowly toward large (more bound) energies: in other words, most of the disruptions occur from orbits within the gravitational influence sphere, regardless of the value of M_\bullet . The plot of $q(\mathcal{E})$ shows that, for $M_\bullet \approx 10^8 M_\odot$, the entire influence sphere lies within the empty-loss-cone regime. As M_\bullet is reduced, more and more of the loss cone is full.

For $\{m_\star, R_\star\} = \{M_\odot, R_\odot\}$, the loss rate is well approximated by

$$\begin{aligned} \dot{N}_{\text{SIS}} &\equiv \int F(E) dE \\ &\approx 4.3 \times 10^{-4} \left(\frac{\sigma}{90 \text{ km s}^{-1}} \right)^{7/2} \left(\frac{M_\bullet}{4 \times 10^6 M_\odot} \right)^{-1} \text{ yr}^{-1} \end{aligned} \quad (33)$$

Equation (33), combined with the M_\bullet - σ relation, implies $\dot{N} \sim M_\bullet^{-0.25}$: consumption rates are higher in smaller galaxies—assuming that their NSCs have properties that scale in the assumed way with M_\bullet .

Tidal disruption rates as high as 10^{-4} yr^{-1} in nuclei with $M_\bullet = 10^6 M_\odot$ imply a liberated mass comparable to M_\bullet after 10 Gyr. This is not necessarily a problem, since only a fraction of the gas removed from stars is expected to find its way into the hole [50]. Nevertheless, the high values of \dot{N} predicted for low-luminosity galaxies suggest that matter tidally liberated from stars might contribute substantially to SBH growth in these galaxies. If SBHs are common in dwarf galaxies and in the bulges of late-type spiral galaxies (both very uncertain hypotheses), these systems would dominate the total tidal flaring rate, due both to their large numbers and to their high individual event rates [62].

2.3. Time-dependent loss rates

Loss-cone theory was originally directed toward understanding the observable consequences of massive black holes at the centers of globular clusters [19, 28]. Globular clusters are many relaxation times old, and this assumption was built into the theory, by requiring the stellar phase-space density near the hole to have reached an approximate steady state under the influence of gravitational encounters. Unfortunately, the assumption of a collisionally-relaxed distribution is not likely to be justified in all galactic nuclei. Figure 2 suggests that only nuclei with the smallest SBHs—smaller than the $\sim 4 \times 10^6 M_\odot$ SBH at the Galactic center—are likely to have nuclear relaxation times much shorter than 10 Gyr.

Even in nuclei where the relaxation time is much too long for the distribution of orbital energies to have reached a steady state at $r \lesssim r_h$, the angular momentum distribution of stars near the SBH may have evolved appreciably. § The characteristic time for gravitational encounters to alter the angular momenta of orbits with $L \lesssim L_0$ is

$$t_L \approx \frac{L_0^2}{L_c^2} t_r. \quad (34)$$

§ This is even more true at $r \ll r_h$ where resonant relaxation is effective, as discussed below.

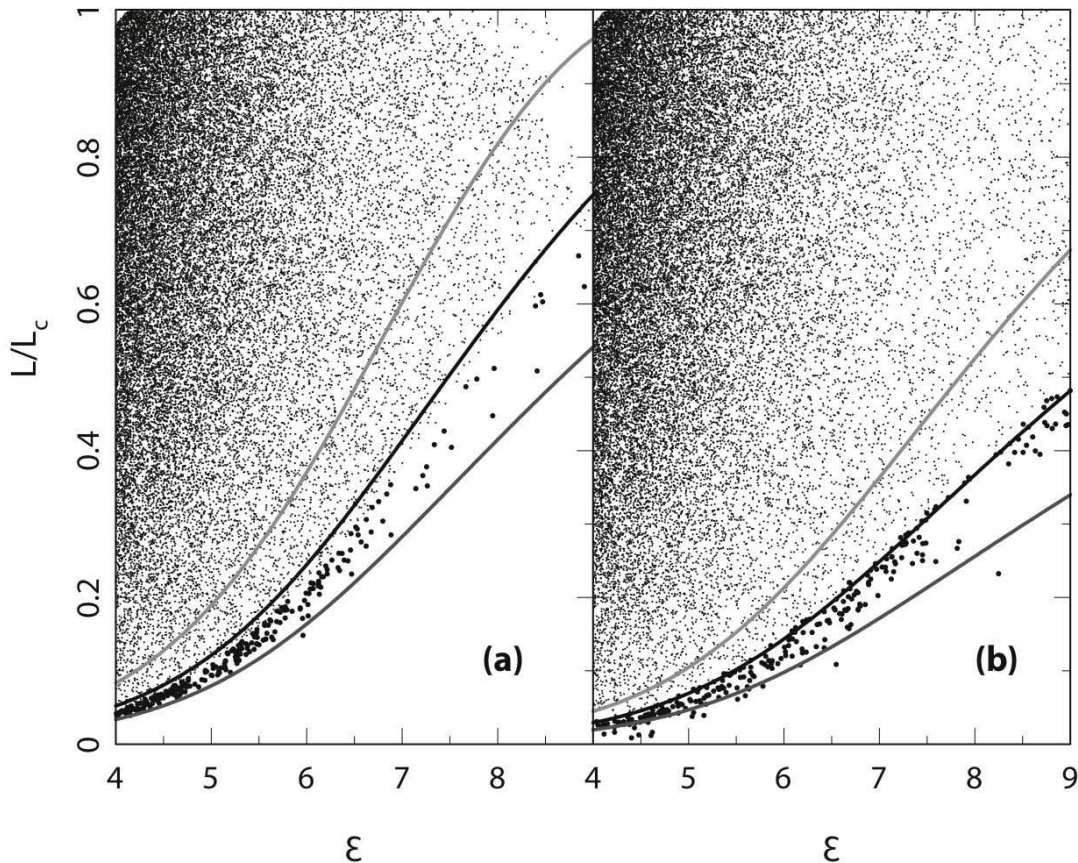


Figure 4. The gap in phase space created by a binary SBH at the center of a galaxy [41]. The binary mass ratios were (a) $M_2/M_1 = 1$ and (b) $M_2/M_1 = 1/8$. Curves show the angular momenta of orbits with periastrons of 0.5, 1, and 2 times a_h . The edge of the gap is approximately coincident with the middle curve in both cases, corresponding to orbits that graze the sphere $r = a_h$. The larger circles are stars that are still interacting with the binary, i.e., stars with periastrons that lie within a few times a_h . These stars may still be ejected via the “secondary slingshot” [42].

If L_0 is equal to L_{lc} , the angular momentum of an orbit with periastris r_{lc} , then $t_L \ll t_r$. But giant galaxies almost universally exhibit “cores,” with sizes 10^1 – 10^2 pc [18, 27, 16], and one widely discussed model attributes cores to the ejection of stars by a binary SBH during a galaxy merger. The massive binary creates a gap in phase space (figure 4) corresponding to orbits that intersected the binary at some point in its evolution from $\Delta r \approx r_h$ to $\Delta r \approx a_h$, where a_h is the “hard binary separation”: the separation at which the two SBHs are close enough together to eject passing stars completely out of the nucleus. N -body simulations [30] suggest $a_h \approx \nu r_m/4$, where $\nu \equiv M_1 M_2 / (M_1 + M_2)^2$ is the reduced mass ratio of the binary and r_m is the influence radius defined above. Replacing L_0^2 by $2GM_\bullet a_h$ in equation (34), and writing $L_c^2 \approx GM_\bullet r_m$, appropriate for stars at a distance $\sim r_m$ from the SBH, yields

$$\frac{t_L}{t_r(r_m)} \approx \frac{2a_h}{r_h} \approx \frac{\nu}{2} \approx \frac{M_2}{2M_1} \quad (35)$$

where the last expression assumes $M_2 \ll M_1$. Combining equation (35) with equation (12) yields

$$t_L \approx 1.5 \times 10^{10} \left(\frac{\nu}{0.1} \right) \left(\frac{M_\bullet}{10^7 M_\odot} \right)^{1.54} \text{ yr.} \quad (36)$$

Equation (36) suggests that the distribution of orbital angular momenta of stars near the SBH should be assumed to be gradually evolving in nuclei with $M_\bullet \gtrsim 10^7 M_\odot$.

Returning to equation (17), and changing variables to $\ell = \sqrt{\mathcal{R}}$, the evolution equation can be written

$$\frac{\partial N}{\partial t} = \frac{\mu}{\ell} \frac{\partial}{\partial \ell} \left(\ell \frac{\partial N}{\partial \ell} \right), \quad \mu(\mathcal{E}) \equiv \frac{\mathcal{D}(\mathcal{E})}{4}. \quad (37)$$

The assumption of diffusive evolution—i.e. that a star’s angular momentum changes very little over one orbital period—is very well satisfied here since $a_h \gg r_t$; in other words, we are almost always in the empty-loss-cone regime. Equation (37) is the heat conduction equation in cylindrical coordinates, with radial variable ℓ and diffusivity μ [43], and the solution can be expressed in terms of a Fourier–Bessel series; the boundary conditions are

$$\left. \frac{\partial N}{\partial \ell} \right|_{\ell=1} = 0 \quad \text{and} \quad N(\mathcal{E}, \ell) = 0, \quad \ell \leq \ell_{\text{lc}}(\mathcal{E}) = \mathcal{R}_{\text{lc}}(\mathcal{E})^{1/2}. \quad (38)$$

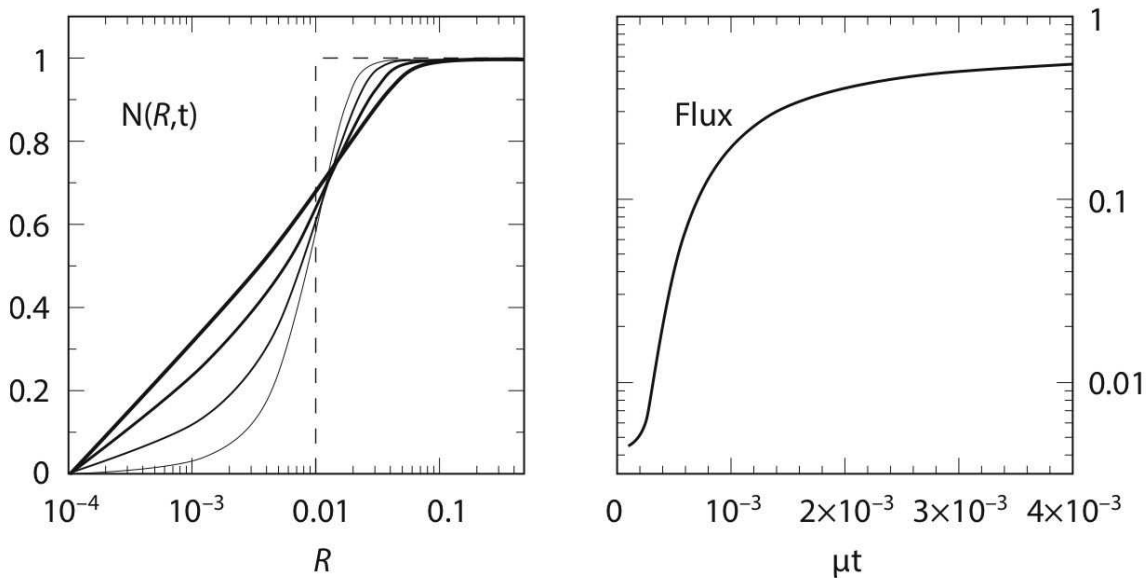


Figure 5. The left panel shows the evolution of $N(\mathcal{E}, \mathcal{R}, t)$ at one \mathcal{E} , computed using equation (37). The right panel shows the flux (per unit of \mathcal{E}) into the loss cone at this \mathcal{E} . The initial $N(\mathcal{R})$ is shown at left as the dashed line: $N(\mathcal{E}, \mathcal{R}, 0) = 0$ for $\mathcal{R} \leq 0.01$. The angular momentum of the loss cone was fixed at $\mathcal{R}_{\text{lc}} = 10^{-4}$. In the left panel, times shown are $\mu t = (0, 0.05, 0.1, 0.2, 0.4) \times 10^{-2}$; line width increases with time. The steady-state solution is nearly reached in a time of $\sim 10^{-2} t_r$, consistent with the estimate of equation (34).

Figure 5 illustrates the evolution described by these equations. The initially steep phase-space gradients decay on the expected timescale of $\sim \mathcal{R}_0 t_r \sim 10^{-2} \mu^{-1}$. At the final time, $N(\mathcal{R})$ has nearly attained the exponential form expected for the steady-state solution outside of an empty loss cone, equation (19).

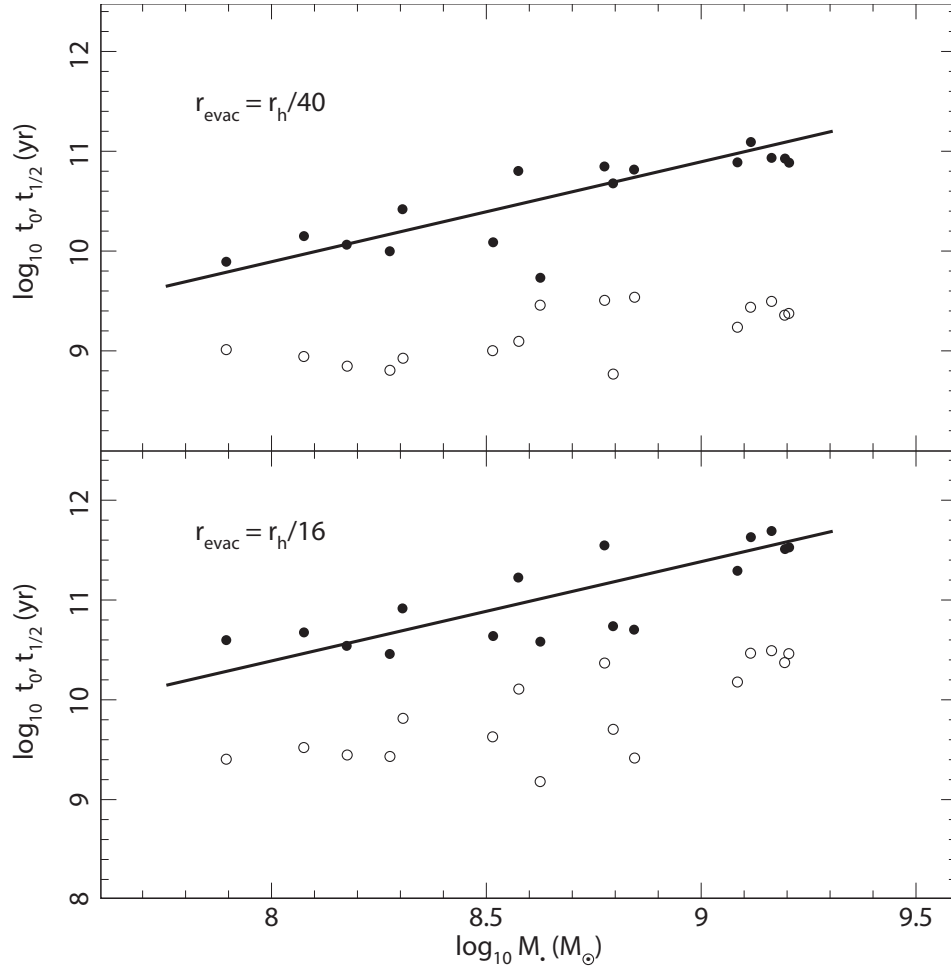


Figure 6. Two characteristic times associated with loss-cone refilling in a sample of elliptical galaxies, assuming spherical symmetry, and that initially no stars were present with periapsides inside r_{evac} [41]. t_0 (open circles) is the elapsed time before the first star is scattered into the loss cone, and $t_{1/2}$ (filled circles) is the time for the loss-cone flux to reach 1/2 of its steady-state value. Solid lines are the approximate fitting function for $t_{1/2}$, equation (39).

Similar calculations can be used to estimate whether loss-cone feeding rates in observed galaxies are likely to be close to their steady-state values [41]. The initial normalization of $N(\mathcal{R})$ at each \mathcal{E} is fixed by the requirement that the *final*, \mathcal{R} -averaged f be equal to the f inferred from the galaxy's luminosity profile, assuming velocity isotropy. Figure 6 shows the results for a sample of elliptical galaxies, and for two values of r_{evac} , assuming that stars are initially absent from orbits with periapsides

inside r_{evac} . The values of r_{evac} are roughly what would be expected if the current SBH were preceded by a binary with mass ratio of 0.1 or 1. Two characteristic times are plotted: the elapsed time before a single star would be scattered into the loss cone; and the time before the flux (integrated over energies) reaches one half of its steady-state value. The latter time is found to be given roughly by

$$\frac{t_{1/2}}{10^{11} \text{ yr}} \approx 4 \frac{r_{\text{evac}}}{r_{\text{h}}} \frac{M_{\bullet}}{10^8 M_{\odot}}. \quad (39)$$

Evidently, it would be dangerous to assume steady-state feeding rates in galaxies with SBHs more massive than $\sim 10^8 M_{\odot}$.

3. Nonspherical nuclei

If orbits were populated at some early time without regard to the presence of a central sink, a certain number of stars would find themselves on loss-cone orbits. Such stars will pass inside r_{lc} simply as a consequence of their unperturbed motion. This process is called “orbit draining”, and in a spherical galaxy that obeys Jeans’s theorem (i.e. in which orbits are uniformly populated with respect to phase), the rate of passage of stars into the SBH due to orbit draining is just equal to the full-loss-cone rate defined above. Orbit draining is usually ignored in the context of spherical galaxies because the number of stars initially on loss-cone orbits is likely to have been small, and because these stars would have been consumed after just one orbital period. But these arguments need to be modified in the case of nonspherical nuclei. Torques from a flattened potential cause orbital angular momenta to change, even in the absence of gravitational encounters. This means that—compared with a spherical nucleus—a potentially much larger fraction of stars can be on orbits that will eventually bring them inside the sphere of destruction. The timescale over which a star on such an orbit passes within r_{lc} is typically long compared with *radial* orbital periods, but it may still be much shorter than the timescale for gravitational encounters to act.

Nonspherical nuclei can be approximated either as axisymmetric or triaxial. In the case of axisymmetric nuclei, orbits conserve the energy E and the component L_z of the angular momentum parallel to the symmetry axis. In the absence of encounters, a necessary condition for a star to find its way into the SBH is $\ell_z \equiv L_z/L_c(E) < \ell_{\text{lc}}$. But it turns out that small- L_z orbits near the SBH need not conserve total angular momentum, even approximately; they are often “saucers,” orbits that are instantaneously close to Keplerian ellipses but whose angular momentum and inclination (defined with respect to the symmetry plane of the nucleus) oscillate in such a way that $\ell_z = \ell \cos i$ is conserved (Figure 7). || The maximum, instantaneous angular momentum of a saucer orbit turns out to be $\ell \approx \epsilon^{1/2} \gg \ell_{\text{lc}}$ where

$$\epsilon \approx \frac{1}{2}(1 - q) \quad (40)$$

|| This behavior is mathematically very similar to the behavior of orbits in the Kozai-Lidov problem, which approximates the force from a massive object via an axisymmetric, time-averaged potential.

and q is the short-to-long axis ratio of the stellar figure [61]. A substantial fraction of stars with $\ell_z < \ell_{lc}$, and with *instantaneous* angular momenta less than $\sim \epsilon^{1/2}$ will pass eventually within r_{lc} . If the population of low- ℓ orbits is not too different from the population in an isotropic, spherical galaxy having the same radial mass distribution, the fraction of stars at any E that are destined to pass within r_{lc} is

$$\sim \int_0^{\ell_{lc}} dl_z \int_0^{\sqrt{\epsilon}} dl \approx \sqrt{\epsilon} \ell_{lc} \quad (41)$$

compared with the smaller fraction $\sim \ell_{lc}^2$ in a spherical galaxy. The timescale over which these orbits are drained is the longer of the radial period and the period, t_{prec} , associated with precession through a full cycle in ℓ or $\cos i$; the latter time is roughly $\sim \epsilon^{-1/2}$ times the ‘‘mass precession time’’ $t_M \approx PM_{\bullet}/M_{\star}$, i.e. the time for apsidal precession of an orbit due to the (spherically) distributed mass. Near the influence radius, $M_{\star} \approx M_{\bullet}$, and in a nucleus of moderate flattening, $\epsilon^{-1/2}t_M$ will be of order or somewhat longer than $P(r_h)$. While longer than the time required for loss-cone draining in spherical galaxies, this time is still short enough that the saucer orbits within $\sim r_h$ would probably be drained soon after the SBH is in place.

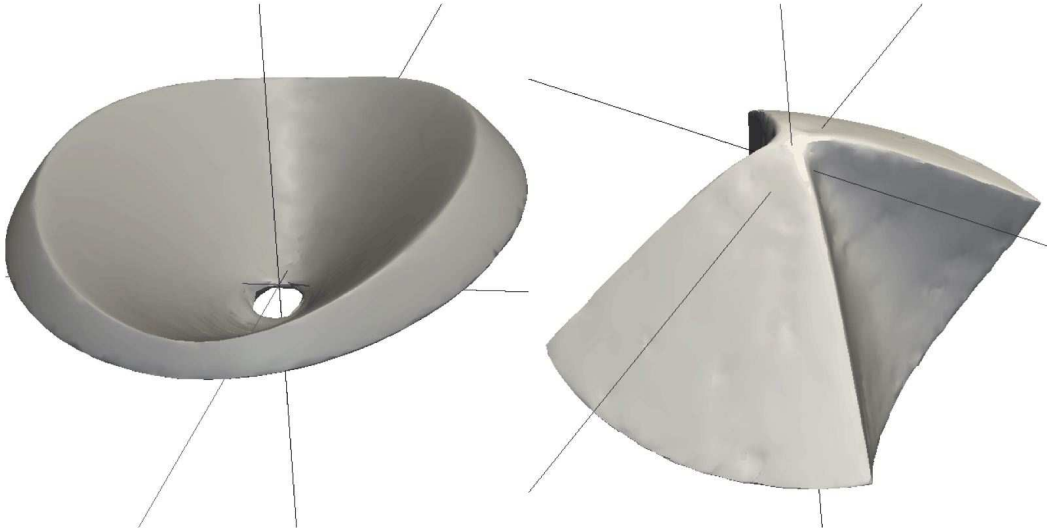


Figure 7. Two important types of orbit that exist near SBHs in axisymmetric or triaxial nuclei. *Left:* saucer orbit; *right:* pyramid orbit. Each figure shows the surface of the three-dimensional volume filled by the orbit; the SBH is at the origin and the short (z) axis of the nucleus is indicated by the vertical line. Saucer orbits are present in both axisymmetric and triaxial nuclei; their excursions in L are limited to $L \geq L_{\min}$, where $L_{\min} = L_z$ in the axisymmetric case. Pyramid orbits exist only in the triaxial geometry; they reach zero angular momentum at the corners of the pyramid. Both types of orbit have counterparts obtained by reflection about a symmetry plane of the potential.

Saucer-like orbits exist also in triaxial nuclei [53], but much of the phase space in triaxial potentials is occupied by an additional family of orbits: the pyramid orbits [38],

which can be modeled as eccentric Kepler ellipses that precess, in two directions, about the short axis of the triaxial figure [39]. The angular momentum of a pyramid orbit reaches zero at the corners of the “pyramid,” and so *every* star on a pyramid orbit will eventually pass within r_{lc} ¶ —unlike saucer orbits, which are limited by conservation of ℓ_z to a minimum radius of periapsis. A fraction of order ϵ of stars in a triaxial nucleus may be on pyramid orbits—larger than the fractions $\sim \ell_{lc}^2$ or $\sim \sqrt{\epsilon}\ell_{lc}$ of stars in spherical or axisymmetric nuclei that pass within r_{lc} . But the time required for a star on a pyramid orbit to reach a given $\ell = \ell_{lc} \ll 1$ can be much longer than for saucers, since the angular momentum of a pyramid orbit oscillates with two independent frequencies; the proportion of time that an orbit has $\ell < \ell_{lc}$ is roughly $(\ell_{lc}/\ell_0)^2$ where ℓ_0 is the orbit’s typical angular momentum. The capture time is long enough that some stars on pyramid orbits, even within r_h , can be expected to survive for times comparable to galaxy lifetimes.

Geometry	Spherical	Axisymmetric	Triaxial
Fraction of stars			
with $\ell_{\min} < \ell_{lc}$	ℓ_{lc}^2	$\sqrt{\epsilon}\ell_{lc}$	ϵ
Draining time	P	$\gtrsim t_{\text{prec}}$	$\gg t_{\text{prec}}$

Table 3 compares the different geometries. It is reasonable to assume that the feeding of SBHs in spherical galaxies is dominated by gravitational scattering, as discussed above, while in triaxial galaxies gravitational encounters are of secondary importance compared with the draining of centrophilic orbits like the pyramids. Precisely axisymmetric nuclei are problematic. It has been argued [29] that feeding rates in axisymmetric galaxies can be dominated by orbit draining, even at very late times ($\gtrsim 10$ Gyr) after formation of the SBH, implying capture rates that are essentially the same as in fully triaxial galaxies. This argument assumes that there exists in axisymmetric potentials a substantial population of chaotic orbits at $r \gg r_h$ and that these orbits are not drained at some early time. Whether or not these assumptions are correct, gravitational *scattering* of stars into the loss cone in axisymmetric nuclei will be affected by the presence of the saucers, even after draining is complete, implying modestly larger ($\sim 2\times$) capture rates than in equivalent spherical nuclei [61]. We discuss each case in more detail below.

3.1. Axisymmetric nuclei

Orbits near the SBH in axisymmetric nuclei fall into one of two families, the tubes and the saucers. Except near the separatrices dividing the two families, tube orbits behave in a manner similar to the annular orbits in spherical potentials: the amplitude of the total angular momentum, L , is nearly fixed, and there is a minimum distance of closest

¶ In the absence of relativistic effects.

approach to the SBH that is related to this nearly constant L by an equation similar to (3). Saucer orbits, on the other hand, can exhibit large angular momentum variations. Saucer orbits exist for

$$\ell_z \equiv \frac{L_z}{L_c(E)} < \ell_{\text{sep}} \approx \sqrt{\epsilon} \quad (42)$$

with ϵ defined, as above, in terms of the nuclear shape. When L_z satisfies this condition, there exists a one-parameter set of saucer orbits at the specified E defined by the third integral H , or equivalently by the maximum and minimum values of ℓ , $\{\ell_+, \ell_-\}$, reached during a single period of oscillation in ℓ and i . In one class of nuclear models – in which the density falls off as a power of radius – the third integral is given approximately by [61]

$$H(\ell, \omega) = (\ell^2 - \ell_z^2) \left(1 - \frac{\ell_{\text{sep}}^2}{1 - \ell_{\text{sep}}^2} \frac{1 - \ell^2}{\ell^2} \sin^2 \omega \right) \quad (43)$$

with ω the argument of periapsis of the osculating Keplerian ellipse; equation (43) shows that $H \approx \ell^2$ for tube orbits with $\ell \gg \ell_z$, and furthermore $H > 0$ for tubes and $H < 0$ for saucers.

On the separatrix, $\ell_+ = \ell_{\text{sep}}$ and $\ell_- = \ell_z$; away from the separatrix the variations in ℓ are smaller, and they are zero for the fixed-point orbit, which has $\ell_{\text{f.p.}}^2 \approx \sqrt{\epsilon} \ell_z$, $(\cos i)_{\text{f.p.}}^2 \approx \ell_z / \sqrt{\epsilon}$ (Figure 8). The period of oscillation in ℓ is very long near the separatrix but drops rapidly away from it, with a typical value of $\sim \epsilon^{-1/2}$ times the mass precession time t_M : longer than orbital periods, but probably shorter than the timescale for gravitational encounters to change L or L_z .

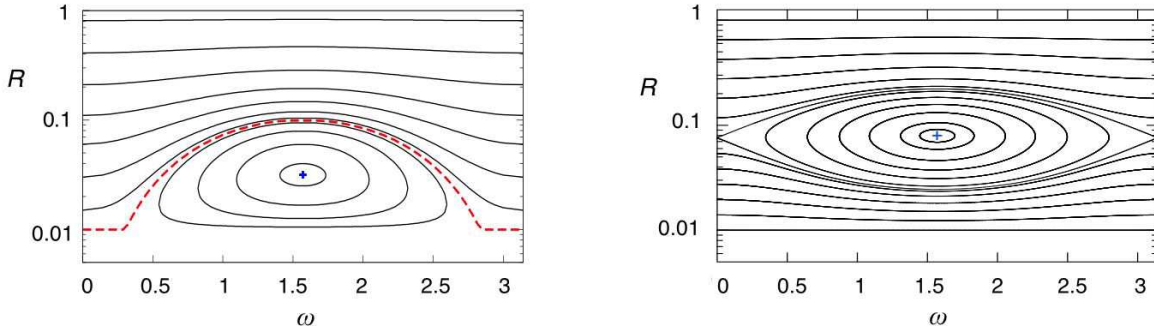


Figure 8. Angular momentum ($\mathcal{R} = L^2/L_c^2 = \ell^2$) vs. argument of periapsis ω for orbits near the SBH in an axisymmetric nucleus. Each panel shows phase diagrams for orbits with the same E and L_z but different values of the “third integral” H (equation 43). *Left:* $\mathcal{R}_z = 0.01$, $\mathcal{R}_{\text{sep}} = 0.1$; the fixed point orbit is marked with a cross and the separatrix with the dashed red line. Orbits above the separatrix are tubes and orbits below are saucers. *Right:* $\mathcal{R}_z = 0.01$ and $\kappa = 0.02$ where κ measures the importance of relativity (eq. 45). An additional family of tube orbits exists below the fixed point, which have sufficiently small L that relativistic precession quenches the effects of torques due to the flattened potential. When κ is increased to ~ 1 , saucer-like orbits disappear completely.

In the spherical geometry, an orbit must satisfy $L < L_{\text{lc}}$ if the star is to go into the SBH. In the axisymmetric geometry, some fraction of the orbits satisfying the weaker condition $L_z < L_{\text{lc}}$ can be captured at each E ; this fraction is roughly the fraction of orbits, in a spherical potential, that would have $L < L_{\text{sep}}$. Since L_{sep} is typically much greater than L_{lc} , the number of stars available for capture can be much larger than in the spherical case. The “loss wedge” [29] is defined as the set of orbits that can be captured in the absence of relaxation; that is, orbits which, at some point in their (ℓ, ω) precessional cycle, attain $\ell \leq \ell_{\text{lc}}$. The name refers to the fact that this region is elongated in the L direction (more precisely, in the direction of the third integral H) much more than in L_z (Figure 9).

To lowest post-Newtonian order, general relativity affects the motion by inducing apsidal (also called geodetic, de Sitter, or Schwarzschild) precession at an orbit-averaged rate

$$\left| \frac{d\omega}{dt} \right|_S = \frac{6\pi}{P} \frac{GM_\bullet}{c^2 a (1 - e^2)} = \frac{3(GM_\bullet)^{3/2}}{c^2 a^{5/2} \ell^2} = 3 \frac{r_g \nu_r}{a \ell^2} \quad (44)$$

where $\nu_r \equiv 2\pi/P$ is the radial (Keplerian) frequency and $r_g \equiv GM_\bullet/c^2$. For orbits of a given E , i.e. a , the effects of GR precession on the motion can be characterized in terms of the dimensionless parameter

$$\kappa(a) = \frac{3r_g}{a} \frac{M_\bullet}{M_\star(r < a)}, \quad (45)$$

approximately the ratio of the GR precession frequency to the mass precession frequency for a low-eccentricity orbit. Saucer-like orbits are only present for $\kappa \lesssim 1$, i.e. if

$$\frac{a}{r_g} \gtrsim 3 \frac{M_\bullet}{M_\star(a)} \quad (46)$$

which for the density model of equation (31) implies

$$a \gtrsim \frac{c}{\sigma} r_g \approx 10^{-2} \left(\frac{M_\bullet}{10^8 M_\odot} \right) \left(\frac{\sigma}{200 \text{ km s}^{-1}} \right)^{-1} \text{ pc}. \quad (47)$$

Even when saucers are present, GR precession limits their minimum angular momenta to

$$\ell_{\text{min}} \approx \frac{2}{3\pi} \frac{\kappa}{\epsilon}. \quad (48)$$

Requiring that $\ell_{\text{min}} \lesssim 4\sqrt{r_g/a}$, we obtain a condition for a star on a saucer orbit to be captured by the SBH:

$$a \gtrsim \left(\frac{1}{2\pi\epsilon} \frac{\sigma}{c} \right)^{2/3} r_m \approx 0.05 \left(\frac{\epsilon}{0.01} \right)^{-2/3} \left(\frac{\sigma}{200 \text{ km s}^{-1}} \right)^{2/3} r_m. \quad (49)$$

(Of course, at smaller radii, there may still be tube-like orbits with sufficiently small L .) The radius of equation (49) is small enough that the effects of relativity can typically be neglected in the axisymmetric loss-cone problem, at least in the context of tidal destruction of main sequence stars; however GR becomes crucial at the smaller radii from which compact stellar remnants would be captured, as discussed below.

The encounter-driven flux of stars into the loss wedge (per unit of energy), \mathcal{F}_{lw} , is given by an expression like

$$\mathcal{F}_{\text{lw}} = - \int_{H_{\text{lc,f.p.}}}^{\mathcal{R}_{\text{capt}}} F^{\mathcal{R}_z} dH - \int_0^{\mathcal{R}_{\text{capt}}} (F_{\text{tube}}^H - F_{\text{saucer}}^H) d\mathcal{R}_z. \quad (50)$$

Here F^H and $F^{\mathcal{R}_z}$ are fluxes in the H and \mathcal{R}_z directions respectively, $H_{\text{lc,f.p.}}$ is the lowest possible value of H for orbits outside the loss wedge, and the two terms in the last integral give the contributions to the capture rate from the “downward” flux in the H direction in the tube region of phase plane and the “upward” flux in the saucer region (see Figure 9).

Just as in the spherical case, however, there are two regimes, depending on whether the radial period P is short or long compared with the time required for an orbit to transit the loss cone. In the axisymmetric geometry, the latter can occur in one of two ways: by scattering, or by orderly precession. Assume—as turns out to be correct—that the latter is more important. Then, if the radial period is shorter than that part of the precessional cycle for which $\ell < \ell_{\text{lc}}$, the star will be captured in a time no longer than t_{prec} . Stars that satisfy this condition can be said to be in the “empty-loss-wedge” regime. In the opposite limit, a star that achieves $\ell < \ell_{\text{lc}}$ while far from periapsis may precess out of the loss cone before capture occurs, similar to what happens in the full-loss-cone case of the spherical problem. In this “full-loss-wedge” regime, precession shuffles stars in angular momentum quickly enough that the loss cone remains full, hence the capture rate is just the instantaneous number of stars inside the loss cone divided by their radial period — equivalent to the full-loss-cone draining rate in the spherical geometry. By analogy with the spherical case, the quantity that characterizes the two regimes is q_{axi} , where

$$q_{\text{axi}} \approx \frac{P}{t_{\text{prec}}} \frac{L_{\text{sep}}}{L_{\text{lc}}} \approx \frac{P}{t_{\text{M}}} \frac{L_{\text{sep}}^2}{L_{\text{lc}}} \approx \frac{M_{\star}(a)}{M_{\bullet}} \frac{\epsilon}{\ell_{\text{lc}}}. \quad (51)$$

Note that we are comparing the radial period, P , with the (approximate) time for the orbit to precess through the loss cone, $(\ell_{\text{lc}}/\ell_{\text{sep}})t_{\text{prec}}$. It is easy to see that $q_{\text{axi}} \gg 1$ at the radius of influence, since $P \approx t_{\text{M}}$. Unlike the spherical problem, the transition from empty- to full-loss-wedge regimes always occurs well within the radius of influence, and therefore the main contribution to the total capture rate comes from the full-loss-wedge regime. Moreover, for most realistic cases $q_{\text{axi}} \gg q$ at all radii. In other words: changes in angular momentum near the loss cone boundary are determined by precession and not by relaxation.

Comparing equations (45), (48) and (51) we see that

$$\frac{\ell_{\text{min}}}{\ell_{\text{lc}}} \approx \frac{1}{\Theta q_{\text{axi}}} \quad (52)$$

with Θ defined in equation (2). Roughly speaking, for orbits in the full-loss-cone ($q_{\text{axi}} > 1$) regime, GR will not preclude a star from reaching $\ell \leq \ell_{\text{lc}}$.

The right panel of figure 9 shows stream lines in a quasi-stationary solution to the two-dimensional $(\mathcal{E}, \mathcal{R})$ diffusion problem [61]. More than one-half of the stream lines

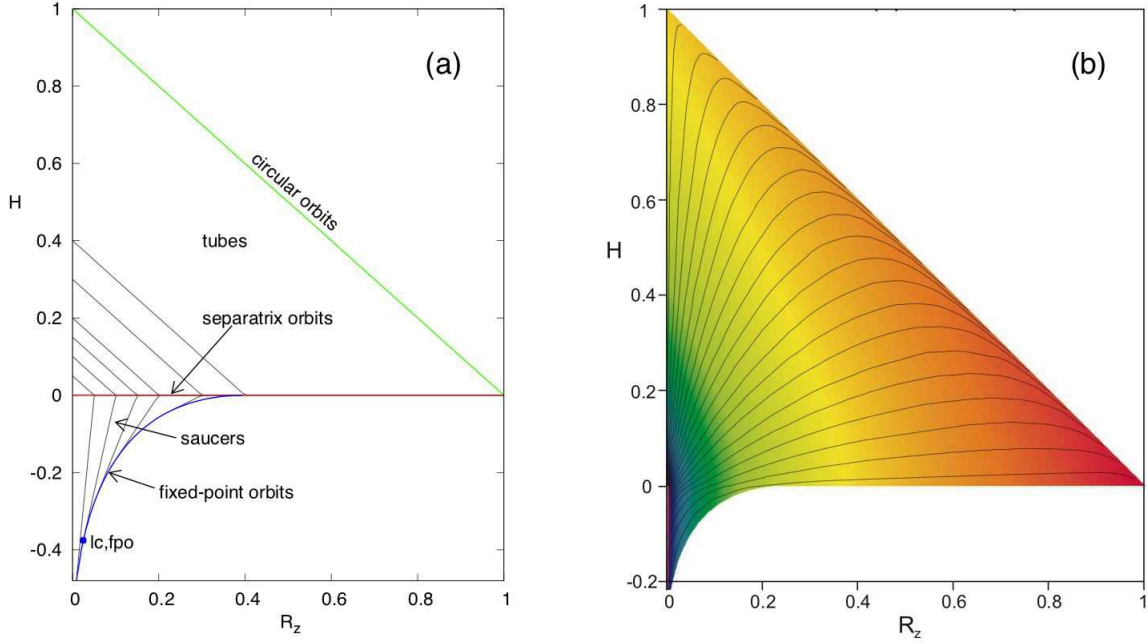


Figure 9. (a) Phase plane in (\mathcal{R}_z, H) coordinates for orbits of a given energy in an axisymmetric nucleus; $\mathcal{R}_z = L_z^2/L_c^2(E) = \ell_z^2$ and H is the “third integral.” The region $0 < H < 1 - \mathcal{R}_z$ is occupied by tube orbits; H is roughly equivalent to L in this region. The bottom left corner is occupied by saucer orbits; the blue curve is the locus of fixed-point saucers. Black lines are loci of constant minimum angular momentum. (b) (\mathcal{R}_z, H) phase plane showing stream lines in a quasi-stationary solution to the two-dimensional diffusion problem. More than one-half of the flux lines end up in the saucer region (at $H < 0$). The steady-state value of f is indicated by the color [61].

end up in the saucer region ($H < 0$). We can obtain an approximate expression for the capture rate if we make a number of simplifying assumptions: (i) the distribution function depends only on the two classical integrals of motion, \mathcal{E} and \mathcal{R}_z ; (ii) the gradient of the distribution function is almost parallel to the \mathcal{R}_z axis in the saucer region and it is in this direction that the diffusion mostly takes place; (iii) precession inside the loss wedge occurs much faster than diffusion, i.e. $q_{\text{axi}} \gg 1$; (iv) the loss wedge is uniformly populated in phase space [29].

Invoking assumptions (i) and (ii), the orbit-averaged equation describing diffusion in L_z is

$$\frac{\partial N}{\partial t} = \frac{\partial}{\partial L_z} (N \langle \Delta L_z \rangle_t) + \frac{1}{2} \frac{\partial^2}{\partial L_z^2} (N \langle (\Delta L_z)^2 \rangle_t) \quad (53)$$

with $N = N(E, L_z)$ the joint distribution of E and L_z . We do not know the true dependence of f on the third integral, but assuming that H is similar to the total angular momentum L , we can write $N(E, L, L_z) dE dL dL_z \approx 4\pi^2 P f dE dL dL_z$ with P the radial period. Integrating this expression with respect to angular momentum from

0 to L_{sep} (the saucer region) then yields

$$N(E, L_z) dE dL_z \approx 4\pi^2 P L_{\text{sep}} f(E, L_z) dE dL_z. \quad (54)$$

Assuming an isotropic field-star distribution, the (local) diffusion coefficients, in the limit of small L_z , are [13]

$$\langle \Delta L_z \rangle = \frac{L_z}{v} \langle \Delta v_{\parallel} \rangle \approx 0, \quad (55a)$$

$$\begin{aligned} \langle (\Delta L_z)^2 \rangle &= \frac{L_z^2}{v^2} \langle (\Delta v_{\parallel})^2 \rangle + \frac{1}{2} \frac{(\varpi^2 v^2 - L_z^2)}{v^2} \langle (\Delta v_{\perp})^2 \rangle \\ &\approx \frac{1}{2} \varpi^2 \langle (\Delta v_{\perp})^2 \rangle \end{aligned} \quad (55b)$$

where ϖ is the cylindrical radius. Recall that in the spherical geometry, diffusion in L at low L is determined by the quantity (18):

$$D(E) \equiv \lim_{\mathcal{R} \rightarrow 0} \frac{\langle (\Delta \mathcal{R})^2 \rangle}{2\mathcal{R}}, \quad (56)$$

the orbit-average of which appears in the spherical diffusion equation (17). Comparing equations (15) and (55b), we can write for the (local) L_z diffusion coefficient

$$\frac{\langle (\Delta L_z)^2 \rangle}{L_c^2} \approx \frac{D}{2} \frac{\varpi^2}{r^2} \approx \frac{D}{2} \sin^2 \theta \quad (57)$$

where θ is the (instantaneous) colatitude. We desire an orbit-averaged expression for this coefficient. For a single, eccentric orbit, θ is nearly independent of the mean anomaly, and so the averaging would be carried out with respect to ω and i . Since we are seeking an estimate of the typical diffusion rate for saucer orbits of specified E and L_z , an additional averaging is required with respect to the third integral. In the absence of detailed knowledge about the distribution over that integral, we simply assume that θ is a uniformly populated variable over its allowed range. Making use of the fact that θ varies nearly from 0 to π for saucers with low L_z (figure 8), we can write

$$\langle (\Delta L_z)^2 \rangle_t \approx \frac{\mathcal{D} L_c^2}{4}. \quad (58)$$

Substituting (54) and (58) into (53) and setting $\partial N / \partial t = 0$, we find $f(E, L_z) = a(E) + b(E)|L_z|$: a linear dependence, rather than the logarithmic dependence characteristic of the spherical (E, L) loss cone. Finally, invoking assumption (iii)—that stars are lost instantaneously after entering the loss wedge—one finds for the flux into the SBH [29]

$$F_{\text{lw}}(E) = \frac{\mathcal{D}(E) \overline{N}(E)}{q(E) + 4L_c(E)/L_{\text{sep}}(E)} \quad (59)$$

where $\overline{N} \equiv \sqrt{2}\pi^3 G^3 M_{\bullet}^3 (-E)^{-5/2} \overline{f}$.

Comparing the fluxes in the spherical and axisymmetric geometries,

$$F \approx F^{\text{max}} \times \begin{cases} [2 \ln(L_c/L_{lc})]^{-1}, & \text{spherical,} \\ (4L_c/L_{\text{sep}})^{-1}, & \text{axisymmetric} \end{cases} \quad (60)$$

where $F^{\text{max}}(E) \equiv N(E)\mathcal{D}(E)$ is an estimate of the maximum rate at which stars can be driven, by gravitational encounters, through a constant-energy surface. The

fraction of stars of energy E that are lost in one relaxation time is $\sim 1/\ln(L_c/L_{lc})$ in the spherical geometry and $\sim L_{sep}/L_c$ in the axisymmetric geometry. The different functional dependencies reflect the fact that diffusion is two-dimensional in the spherical case and effectively one-dimensional in the axisymmetric case [28].

The more complete treatment [61] of two-dimensional (L_z, H) diffusion that was the basis for figure 9b yields steady-state capture rates that are better approximated by

$$F_{lw}(E) = \frac{\mathcal{D}(E) \bar{N}(E)}{\alpha_{axi}(E) + 2 \ln(L_c/L_{sep}) - 1 + 2\pi} \quad (61)$$

where

$$\alpha_{axi} = \begin{cases} q/q_{axi}, & \text{if } q_{axi} < 1, \\ q, & \text{if } q_{axi} > 1 \end{cases} \quad (62)$$

and q_{axi} is given by (51). For the least-bound stars, which are in the full-loss-cone regime, $q_{axi} \gg 1$ and $\alpha_{axi} \approx q \gg 1$. In this case, the capture rate does not depend on the diffusion coefficient \mathcal{D} but only on the value of L_{lc} , as in the spherical problem. In the opposite (diffusive) limit, the feeding rate is higher than in the spherical case, but at most by a factor of a few, a prediction that is confirmed by direct N -body integrations [61].

The results obtained so far assumed regularity of the motion near the SBH. Near and beyond the SBH influence radius, eccentric orbits in axisymmetric potentials tend to be chaotic. Chaotic orbits still respect the two integrals E and L_z , but in principle they can fill the accessible region in the meridional plane, allowing them to be captured as long as $L_z < L_{lc}$. Magorrian and Tremaine [29] suggested that feeding of SBHs by chaotic orbits in axisymmetric potentials might dominate the overall capture rate, especially in the largest galaxies with long central relaxation times.

To a first approximation, one may assume that the chaotic orbits occupy a region in the $L - L_z$ plane with $L < L_{ch}(E)$. The value of L_{ch} plays a role similar to L_{sep} inside the sphere of influence, and in fact is comparable to it for the same degree of flattening. We can estimate the contribution of the chaotic orbits to the feeding rate by assuming also that every chaotic orbit with a given L_z can attain values of $L \in [L_z \dots L_{sep}]$ with equal probability in L^2 . The fraction of time such an orbit spends below the capture boundary is then $\sim (L_{lc} - L_z)/L_{ch}$, and this is essentially the probability of being captured during one radial period. The change with time of f due to capture of stars from chaotic orbits is given approximately by

$$f(L_z, t; E) = f_{init}(L_z; E) \exp \left[-\frac{t}{P(E)} \frac{L_{lc} - L_z}{L_{ch}(E)} \right].$$

The total number of chaotic orbits with $L_z < L_{lc}$ and their capture rate is then given by

$$\begin{aligned} N_{ch}(E, t) dE &= 4\pi^2 \int_0^{\mathcal{R}^{capt}} p(E) f(\mathcal{R}_z, t) (L_{ch}/L_z - 1) d(L_z^2/L_c^2) dE \\ &\approx 8\pi^2 p(E) f_{init} L_{ch} L_{lc} \frac{1 - \exp(-2\tau)}{2\tau} dE, \end{aligned} \quad (63a)$$

$$F_{\text{ch}}(E, t) dE = 4\pi^2 p(E) f_{\text{init}} \frac{1}{P} \left(\frac{L_{\text{lc}}}{L_c} \right)^2 \frac{1 - (2\tau + 1) \exp(-2\tau)}{2\tau^2} dE, \quad (63b)$$

where $p(E) \equiv 2^{-3/2} \pi (GM_\bullet)^3 (-E)^{-5/2}$ and

$$\tau \equiv t/T_{\text{drain}}, \quad T_{\text{drain}} \equiv 2P(L_{\text{ch}}/L_{\text{lc}}). \quad (64)$$

If we identify f_{init} with the initial value of the distribution function in the loss cone, the capture rate is initially equal to the draining rate of a uniformly populated loss cone, equation (26). On the other hand, the draining time depends on L_{ch} since the number of stars in the chaotic region is $2L_{\text{ch}}/L_{\text{lc}}$ times larger than the number of stars in the loss cone, therefore the draining time is longer than the radial period by the same factor. Identifying L_{ch} with L_{sep} , the draining time becomes

$$T_{\text{drain}} \approx P \left(\frac{2\epsilon a}{r_{\text{lc}}} \right)^{1/2} \quad (65a)$$

$$\approx 6 \times 10^{10} \left(\frac{\epsilon}{\Theta} \right)^{1/2} \left(\frac{a}{10^2 \text{ pc}} \right)^2 \left(\frac{M_\bullet}{10^8 M_\odot} \right)^{-1} \text{ yr}, \quad (65b)$$

potentially longer than a Hubble time. At times much longer than the draining time, the capture rate declines as t^{-2} . (For regular orbits within the influence sphere, the draining rate declines as t^{-3} , but the draining *time* for saucer orbits is probably much shorter than a Hubble time.) It follows that the capture rate for stars on chaotic orbits can remain high even in the absence of relaxation, provided that the initial value f_{init} of the distribution function inside the chaotic region was not much different from its value in an isotropic galaxy. Whether this is likely to be true is open to debate; among other things, f_{init} must depend on the details of the galaxy formation process (dissipative *vs.* dissipationless), the prior evolution of a binary SBH (which might have emptied out a large part of the loss wedge via the gravitational slingshot), etc.

Figure 10 shows estimates of the capture rate in spherical and axisymmetric galaxies [61]. The left panel is based on solutions to the Fokker-Planck equations (13), (53), assuming two sets of galaxy models: having either steep ($\rho \propto r^{-3/2}$) central density cusps ($M_\bullet \leq 10^8 M_\odot$) or shallower ($\rho \propto r^{-1}$) “cores” ($M_\bullet \geq 10^8 M_\odot$). The M_\bullet - σ relation:

$$\log M_\bullet = \alpha + \beta \log(\sigma/200 \text{ km s}^{-1}) \quad (66)$$

with $(\alpha, \beta) = (8, 4.5)$ was used to relate M_\bullet to the properties of the galaxy. Solid red and dashed purple lines are stationary and time-dependent rates in the spherical geometry; the time-dependent solutions assumed initial condition with strong gradients in the distribution function near the loss region (as in figure 5), which provide an upper limit to the likely rates in real spherical galaxies. The dot-dashed and dotted blue lines show the same for axisymmetric galaxies with $\mathcal{R}_{\text{sep}} = 0.1$. The double-dashed blue line includes an estimate of the contribution from draining of chaotic orbits. Over the entire range of M_\bullet , the steady-state capture rates differ by only a factor of 2–3 between spherical and axisymmetric geometries, consistent with the discussion above. This result

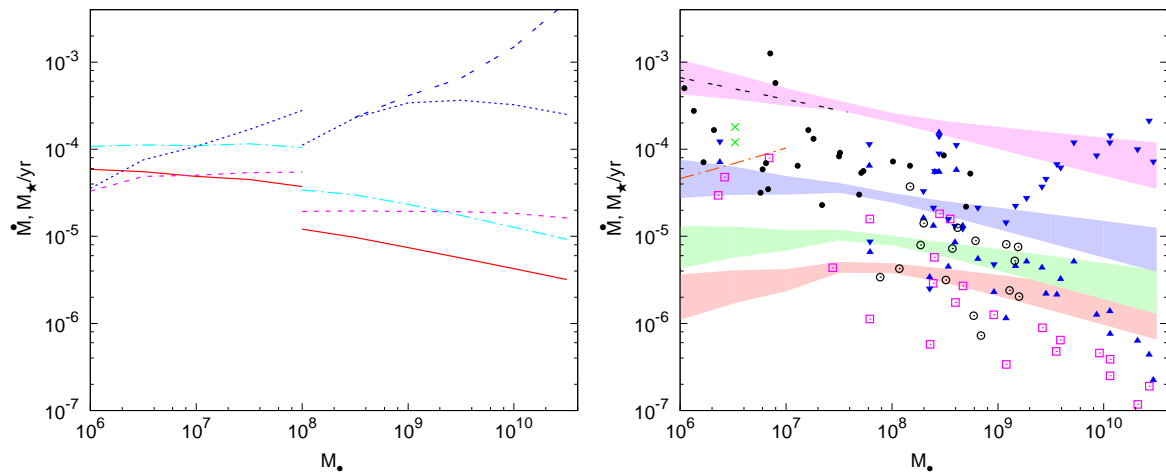


Figure 10. Estimates of the capture rate \dot{M} in spherical and axisymmetric galaxies [61]. Left panel shows stationary and time-dependent solutions to the Fokker-Planck equation; details are given in the text. Shaded bands in the right panel show the dependence of the capture rate in the spherical geometry on uncertainties in the parameters (α, β) that appear in the $M_\bullet - \sigma$ relation; from top to bottom, the nuclear density slope is $\gamma \equiv -d \log \rho / d \log r = (2, 1.5, 1, 0.5)$. Symbols are estimates of capture rates in individual galaxies from previous studies: [59] purple open boxes; [29] blue upward and downward triangles for the spherical and axisymmetric cases respectively; [62] black open and filled circles for cored and cuspy galaxies respectively. Black double-dashed line is equation (33), and red dot-dashed line is based on N -body simulations [6].

holds for any, reasonable galaxy model and depends only weakly on L_{sep} . In the time-dependent solutions, the approach to a steady state is slow and the flux at early stages is much higher than in equilibrium, particularly in the most massive galaxies with long central relaxation times. Also for the most massive SBHs ($M_\bullet \gtrsim 10^9 M_\odot$) the draining time of the loss region becomes comparable to the Hubble time and the capture rate is dominated by chaotic orbits, reaching values up to $10^{-3} M_\odot \text{ yr}^{-1}$ for the largest M_\bullet . As discussed above, the time-dependent results should be considered contingent on the poorly-known initial conditions.

The right panel of Figure 10 plots variation in the stationary, spherical capture rate due to uncertainties in the parameters (α, β) in the $M_\bullet - \sigma$ relation; values for the axisymmetric geometry scale roughly in proportion. The shaded regions, from top to bottom, have $\gamma \equiv -d \log \rho / d \log r = (2, 1.5, 1, 0.5)$. Estimates of the capture rates in individual galaxies from several previous studies are also plotted as symbols. It is clear that the scatter in the derived values is fairly large, about two orders of magnitude, although a general trend of decreasing rate with increasing M_\bullet is clear. Overall, predicted capture rates lie in the range $10^{-5} - 10^{-4} M_\odot \text{ yr}^{-1}$ for less massive galaxies, and a few $\times 10^{-6} - 10^{-5} M_\odot \text{ yr}^{-1}$ for galaxies with $M_\bullet > 10^8 M_\odot$. (Axisymmetric) nuclear flattening may increase these numbers by a factor of few.

One potentially important feature of axisymmetric (and triaxial) galaxies is that most stars are consumed in the full-loss-cone regime. This means that stars approach

the SBH with a wide distribution in periapsis radii, as opposed to “barely touching” the disruption sphere in the empty-loss-cone regime. One consequence is that stars can be strongly tidally distorted before disruption. In the exchange model discussed below for the formation of the Galactic center S-stars from binary stars, the radial distribution of the captured stars depends differently on the initial distribution of binary separations in the empty- and full-loss-cone cases [44].

3.2. Triaxial nuclei

The tube and saucer orbits that characterize motion near an SBH in axisymmetric nuclei are still present in nonaxisymmetric, or triaxial, nuclei. In fact, two families of tube orbits exist, circulating about both the short and long axes of the triaxial figure, as well as saucers that circulate about the short axis [53]. Like orbits in the axisymmetric geometry, tube (saucer) orbits in triaxial potentials respect an integral that is similar to L (L_z) and they avoid the very center. But triaxial potentials can also support orbits that are qualitatively different from both tubes and saucers: “centrophilic” orbits that pass arbitrarily close to the SBH (figure 7).

Centrophilic orbits exist even in axisymmetric nuclei, but they are restricted to a meridional plane, that is, to a plane that contains the z - (symmetry) axis. Orbits in the meridional plane have $L_z = 0$, and so conservation of L_z does not impose any additional restriction on the motion. Perturbing such an orbit *out* of the meridional plane implies a nonzero L_z : the orbit is converted into a saucer or a tube and again avoids the center. But in the triaxial geometry, L_z is not conserved, and it turns out that a substantial fraction of such “perturbed” planar orbits will maintain their centrophilic character, becoming pyramid orbits [38].

Pyramid orbits resemble eccentric Keplerian ellipses that librate in two directions about the short axis of the triaxial figure [39]. In the absence of any nonspherical component to the potential, they would precess at a constant rate

$$\frac{d\omega}{dt} \approx -\nu_r \sqrt{1 - e^2} \left[\frac{M_\star(r < a)}{M_\bullet} \right], \quad (67)$$

[33], the rate of apsidal precession due to the spherically-distributed mass M_\star . But because of the torques due to the triaxial geometry, the orbit’s angular momentum varies as it precesses, from a maximum when the orbit is near the short (z) axis. It is clear that – by making the eccentricity along this axis sufficiently large – it will always be possible to reach $e = 1$ at a finite angle, since the precession period (and hence the accumulated effect of the torques) can be made arbitrarily large. The angles where $e = 1$ correspond to the four “corners” of the pyramid (figure 11). At a given energy E there is a two-parameter family of pyramids defined by the two non-classical integrals U and W , or equivalently by the (x, y) dimensions of the base of the pyramid. Only orbits with peak angular momenta (near the z axis) $\ell \lesssim \sqrt{\epsilon}$ will be pyramids; orbits with larger ℓ never reach $\ell = 0$ and so continue to precess in the same direction, producing saucers or tubes.

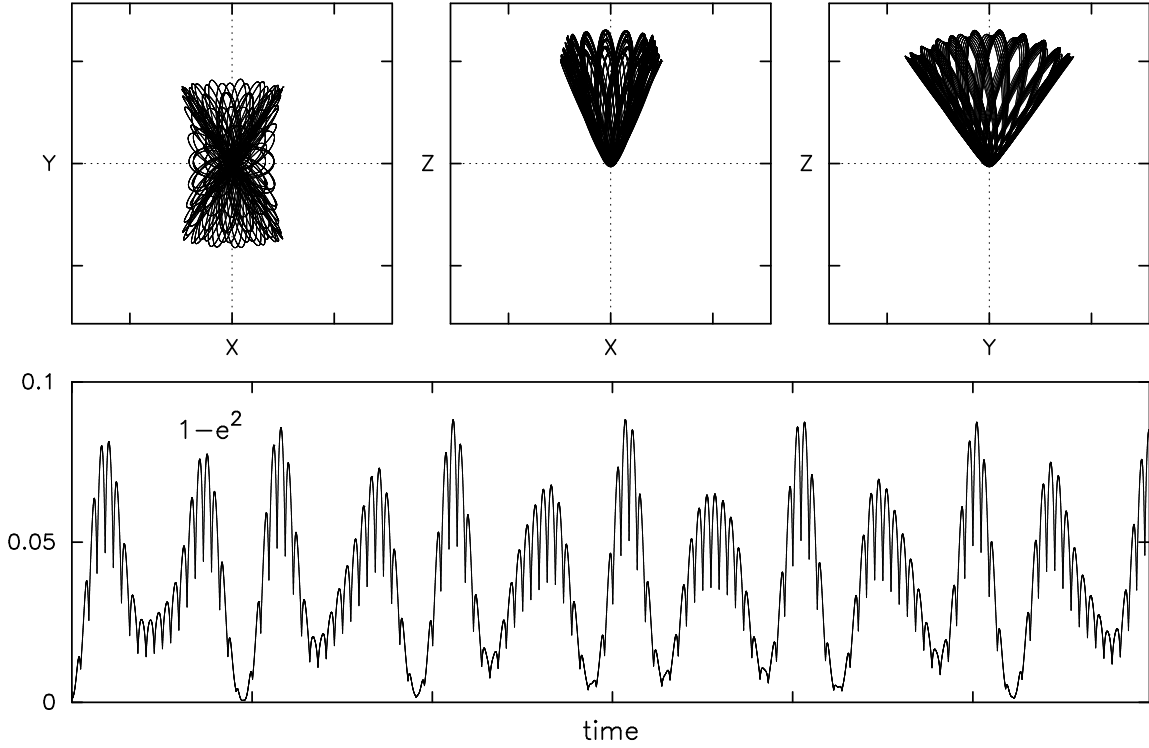


Figure 11. *Top:* A pyramid orbit, seen in three projections. The z -axis is the short axis of the triaxial figure and the SBH is at the origin. *Bottom:* $\ell^2 = 1 - e^2$ versus time, where e is the eccentricity. The eccentricity tends to unity when the orbit reaches the corners of the pyramid's base. Because the frequencies of libration in x and y are generally incommensurate, the corners are only reached after many libration periods.

In the large-eccentricity limit, the additional integrals can be expressed simply in terms of the components of a unit vector, \mathbf{u} , oriented toward the corners of the pyramid:

$$U = \nu_x^2 u_{x0}^2 + \nu_y^2 u_{y0}^2, \quad W = \nu_x^4 u_{x0}^2 + \nu_y^4 u_{y0}^2 \quad (68)$$

where

$$\nu_x = \sqrt{\frac{5\epsilon_c}{3}}, \quad \nu_y = \sqrt{\frac{5}{3}(\epsilon_c - \epsilon_b)} \quad (69)$$

and (ϵ_b, ϵ_c) specify the axis ratios of the triaxial figure through

$$\epsilon_{b,c} \simeq (T_{y,z} - T_x) \frac{\rho_t}{\rho_0} \left(\frac{a}{r_0} \right)^\gamma. \quad (70)$$

In deriving these expressions, the stellar potential was assumed to consist of two parts: a spherical component with density $\rho_s(r) = \rho_0(r/r_0)^{-\gamma}$, and a homogeneous triaxial bar with density ρ_t and potential

$$\Phi_t(x, y, z) = 2\pi G\rho_t (T_x x^2 + T_y y^2 + T_z z^2) \quad (71)$$

where the T_i are expressible in terms of the two axis ratios [8]. Note that in this model, the relative contribution of the triaxial distortion to the total stellar potential is an increasing function of radius.

Pyramids that are sufficiently eccentric (i.e. that have sufficiently compact bases) librate in x and y as harmonic and uncoupled oscillators:

$$u_x(\tau) = u_{x0} \cos(\nu_x \tau + \phi_x), \quad u_y(\tau) = u_{y0} \cos(\nu_y \tau + \phi_y) \quad (72)$$

and their angular momentum varies as

$$\ell^2(\tau) = \ell_{x0}^2 \sin^2(\nu_x \tau + \phi_x) + \ell_{y0}^2 \sin^2(\nu_y \tau + \phi_y) \quad (73)$$

where $\tau \equiv \nu_M t / 3$ and

$$\ell_{x0} = \nu_x e_{x0} / 3, \quad \ell_{y0} = \nu_y e_{y0} / 3. \quad (74a)$$

As long as the frequencies of oscillation in x and y are incommensurable, the vector (u_x, u_y) densely fills the available area, and the star comes close to the SBH whenever the two variables (u_x, u_y) are simultaneously close to 1—that is, near the corners of the pyramid. To the extent that the simple harmonic oscillator approximation is valid, the time-averaged probability of a given periapsis passage having $r_{\text{peri}} < X$ is roughly proportional to X .

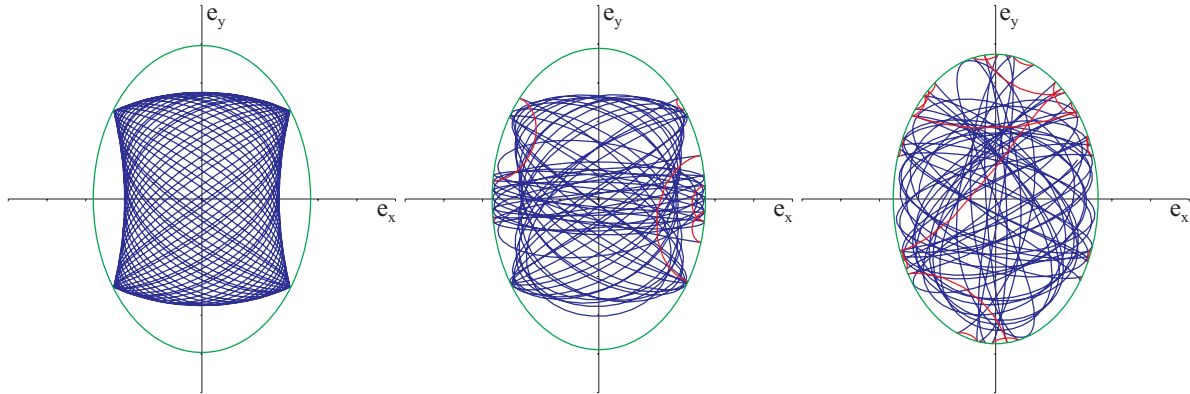


Figure 12. The effect of relativistic precession on pyramid orbits [39]. The three orbits were started with the same initial conditions, but with different values of the coefficient κ (equation 45) that determines the relative speed of relativistic and Newtonian precessions. Left: $\kappa = 0$ (regular); middle: $\kappa = 10^{-6}$ (weakly chaotic); right: $\kappa = 10^{-5}$ (strongly chaotic). The outer ellipse marks the maximal extent of the (u_x, u_y) vector; red segments correspond to $\ell < \ell_{\text{crit}}$, blue to $\ell > \ell_{\text{crit}}$ and to the nonrelativistic case.

Addition of the 1PN relativistic terms to the equations of motion has a similar effect on pyramids as on saucers: it limits the minimum angular momentum attainable by a pyramid orbit, and defines a region very near the SBH where no pyramids can exist. Equations (45) – (49), which were derived for saucer orbits in axisymmetric nuclei, are approximately valid for pyramid orbits if ϵ is identified with $\{\epsilon_b, \epsilon_c\}$. One difference is integrability: pyramid orbits conserve only E (rather than E and L_z) in the presence of GR and so they tend to be chaotic, increasingly so as κ (equation 45) is increased, i.e. as the distance from the SBH decreases. Instead of touching the equipotential surface at just four points, the outer envelope of a chaotic “pyramid” orbit deforms to match the

equipotential surface (Figure 12). However one finds [39] that the minimum attainable angular momentum is not strongly affected by the chaos and is still given by an equation similar to (48).

In strongly triaxial nuclei, centrophilic orbits like the pyramids can dominate the orbital population of self-consistent models [48], and the mass of stars on pyramid orbits can greatly exceed the mass on loss-cone orbits in the spherical or axisymmetric geometries. A reasonable estimate of the feeding rate in triaxial nuclei can be obtained by simply ignoring collisional loss-cone refilling and counting the rate at which stars on centrophilic orbits pass within a distance r_{lc} from the SBH [37]. The neglect of relaxation is likely to be especially justified in the case of the largest galaxies with the longest central relaxation times.

As in the case of saucer orbits in the axisymmetric geometry, pyramid orbits can precess past the loss cone in a time that is either less than, or greater than, a radial period. In the former case, the star has only a finite chance of capture while in the latter case the star is guaranteed to pass through periapsis before the orbit exits the loss cone. The quantity that characterizes the two regimes is [39]

$$q_{\text{tri}} \equiv \frac{\Delta\psi}{2\ell_{lc}} = \frac{P\nu_M}{18\ell_{lc}}\sqrt{W} \quad (75)$$

where $\Delta\psi$ is the angle traversed in a radial period P . If we consider a “typical” pyramid orbit ($u_{x0} \approx u_{y0}$) in a “typical” triaxial nucleus ($\epsilon_b \approx \epsilon_c$) having peak angular momentum (near the z axis) of ℓ_0 , its draining time becomes [39]

$$t_{\text{drain}} \approx \begin{cases} \frac{1}{\sqrt{2}} \frac{\ell_0}{g(q_{\text{tri}})\ell_{lc}} t_{\text{pyr}} & \text{for } 0 \leq q_{\text{tri}} \leq 1, \\ \frac{q_{\text{tri}}}{\sqrt{2}} \frac{\ell_0}{\ell_{lc}} t_{\text{pyr}} & \text{for } q_{\text{tri}} > 1 \end{cases} \quad (76)$$

where

$$g(x) \equiv \frac{2}{\pi} \left[\sqrt{1-x^2} + x^{-1} \sin^{-1}(x) \right]; \quad g(0) = \frac{4}{\pi}, \quad g(1) = 1 \quad (77)$$

and t_{pyr} is the period of a full libration cycle in x or y , which for eccentric pyramids is

$$t_{\text{pyr}} \approx \frac{2\pi}{\nu_M} \frac{1}{\nu_{x,y}} \approx \frac{t_M}{\sqrt{\epsilon}}. \quad (78)$$

Since the maximal ℓ_0 for pyramids is $\sim \sqrt{\epsilon}$, the draining time in the “empty-loss-cone” regime ($q < 1$) is a factor $\sim \sqrt{\epsilon}/\ell_{lc}$ longer than the pyramid precessional period, or $\sim \ell_{lc}^{-1}$ longer than the typical mass precession time PM_{\bullet}/M_{\star} . These inequalities reflect the fact that capture only occurs near the corners of the pyramid, when oscillations in both x and y are simultaneously near their peaks, and less often than once per full libration period in either x or y .

The minimum angular momentum attainable in the presence of GR is expressible in terms of q_{tri} by a relation similar to equation (52):

$$\frac{\ell_{\text{min}}}{\ell_{lc}} \approx \frac{3\pi}{\Theta} q_{\text{tri}}^{-1}. \quad (79)$$

Roughly speaking, the condition that stars be captured is equivalent to the statement that the loss cone is full.

If $\eta_{\text{pyr}}(E)$ is the fraction of stars at energy E that are on pyramid orbits, and $N(E)dE$ the total number of stars at energies E to $E + dE$, the differential loss rate can be written approximately as

$$\begin{aligned} \dot{N}(E) &\approx \eta_{\text{pyr}} N t_{\text{drain}}^{-1} \\ &\approx \eta_{\text{pyr}} \frac{M_{\star}}{M_{\bullet}} \ell_{\text{lc}} \frac{N}{P} \quad \text{for } 0 \leq q \leq 1, \\ &\approx q_{\text{tri}}^{-1} \eta_{\text{pyr}} \frac{M_{\star}}{M_{\bullet}} \ell_{\text{lc}} \frac{N}{P} \quad \text{for } q > 1. \end{aligned} \quad (80)$$

(These expressions assume $\kappa = 0$.) Recall that in a spherical galaxy, the full-loss-cone capture rate is $\sim \ell_{\text{lc}}^2 N/P$. It is clear from equation (80) that the loss rate due to draining of the pyramids can be comparable to this. Even though the time to drain one pyramid orbit is much longer than P , the number of stars available to be captured in one draining time, $\eta_{\text{pyr}} N$, can be much larger than the number of stars on loss-cone orbits in a spherical galaxy, $\sim \ell_{\text{lc}}^2 N$.

After a time $\sim t_{\text{pyr}}$ some parts of the orbital torus that are entering the loss regions will be empty and the loss rate will drop below equation (80). For small q_{tri} , the orbital torus will become striated, containing strips of nearly zero density interlaced with undepleted regions; the loss rate will exhibit discontinuous jumps whenever a depleted region encounters a loss region and the time to totally empty the torus will depend in a complicated way on the frequency ratio ν_x/ν_y and on ℓ_{lc} . For large q_{tri} , the loss rate will drop more smoothly with time, roughly as an exponential law with time constant t_{drain} .

In the case of pyramid orbits with arbitrary (not necessarily small) opening angles, numerical integrations suggest that the probability of finding an instantaneous ℓ^2 less than some value X is given approximately by $P(\ell^2 < X) \propto X$ for small X , corresponding to a linear probability distribution of periapsis radii, $P(r_{\text{peri}} < r) \propto r$; this is natural if one combines a quadratic distribution of impact parameters at infinity with gravitational focusing [37]. Defining μ for each orbit as $P(\ell^2 < \ell_{\text{lc}}^2)$, one finds that while μ varies greatly from orbit to orbit, its overall distribution over an ensemble of pyramid orbits is roughly

$$P_{\mu}(\mu > Y) \approx \left(\frac{Y}{\mu_{\text{min}}} \right)^{-2}, \quad \mu_{\text{min}} \approx \frac{\ell_{\text{lc}}^2}{2\tilde{\eta}} \quad (81)$$

with $\tilde{\eta}$ the fraction of pyramids among all orbits. The average μ for all pyramid orbits is therefore $\bar{\mu} = 2\mu_{\text{min}}$, and the average fraction of time that an orbit of any ℓ spends inside the loss cone is $\bar{\mu}\tilde{\eta} \simeq \ell_{\text{lc}}^2$ (almost independent of the potential parameters ϵ_b and ϵ_c)—the same number that would result from an isotropic distribution of orbits in a spherically symmetric potential. In other words: until such a time as the centrophilic orbits have been substantially depleted, loss-cone feeding rates should be roughly equal to full-loss-cone rates in the equivalent spherical model.

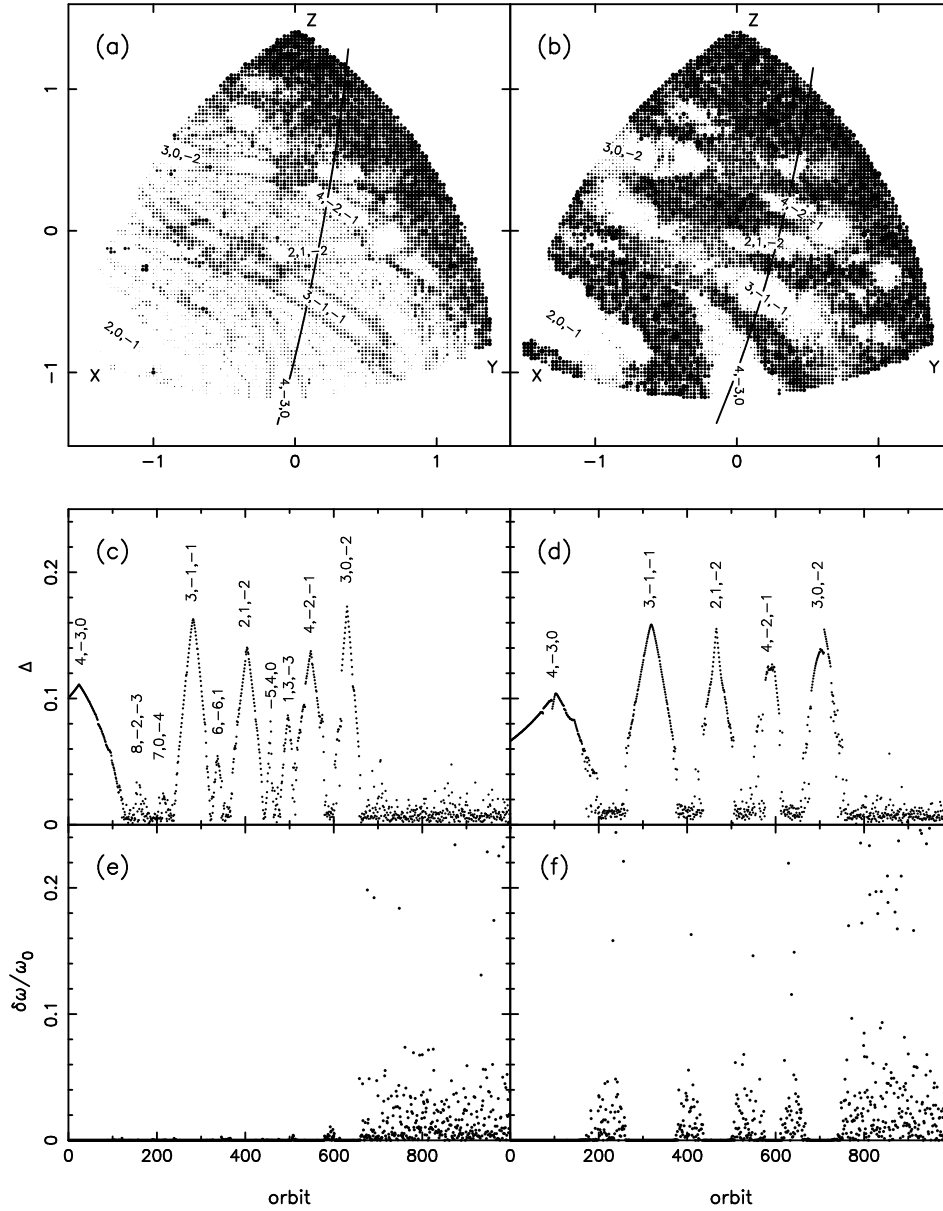


Figure 13. Properties of centrophilic orbits in triaxial galaxies, with (right) and without (left) central SBHs [38]. The top panels show one octant of an equipotential surface located just inside the half-mass radius of the model. Orbits were started on this surface with zero velocity. The top, left, and right corners correspond to the z - (short), x - (long), and y - (intermediate) axes. The gray scale is proportional to the logarithm of the diffusion rate of orbits in frequency space; initial conditions corresponding to regular orbits are white. The most important resonance zones are labeled with their defining integers (m_1, m_2, m_3) . Panels (c) and (d) show the distance of closest approach, Δ , of orbits whose starting points lie along the heavy lines in (a) and (b). The most important stable resonances are again labeled. Panels (e) and (f) show the degree of stochasticity of the orbits, as measured by the change $\delta\omega$ in their “fundamental frequencies”; ω_0 is the frequency of the long-axis orbit and regular orbits have $\delta\omega/\omega_0 = 0$.

As in the axisymmetric case, centrophilic orbits in the triaxial geometry tend to become chaotic near the influence radius where radial and precessional frequencies are comparable. (As noted above, pyramid orbits are also strongly chaotic near the SBH due to GR.) In model potentials with a substantial degree of triaxiality, a “zone of chaos” extends from a few times r_m outward to a radius containing a mass in stars of $\sim 10^2 M_\bullet$ [60]. There are, broadly speaking, two types of centrophilic orbit in this region: regular orbits that avoid passing through the very center, and chaotic orbits. The former orbits lie near to a “thin” orbit, that is, an orbit that respects a resonance between the fundamental frequencies:

$$m_1\nu_1 + m_2\nu_2 + m_3\nu_3 = 0 \quad (82)$$

with the m_i integers. If the parent, resonant orbit avoids the center, orbits that lie close to the resonant torus will do so as well, passing no closer to the center than some minimum distance Δ (figure 13). As the initial conditions move farther from the resonant torus, the orbit broadens, causing it to approach more closely to the destabilizing center. At some critical Δ —typically much larger than r_{lc} —the orbit becomes chaotic. To a good approximation, *all* orbits that pass through the very center and that extend outward into the “zone of chaos” are chaotic.

The complexity of the orbits in this region mandates a brute-force, numerical treatment of SBH feeding [37]. Such calculations are model-dependent but they suggest feeding rates in triaxial galaxies of order

$$\dot{M} \approx 10^{-5} \eta \left(\frac{r_h}{100 \text{ pc}} \right)^{-5/2} \left(\frac{M_\bullet}{10^8 M_\odot} \right)^{5/2} M_\odot \text{ yr}^{-1} \quad (83)$$

with a weak dependence on the degree of triaxiality; here η is the fraction of orbits that are centrophilic. Equation (83) is based on a nuclear model in which $\rho \sim r^{-1}$, not too different from what is observed near the centers of bright elliptical galaxies.

4. Massive perturbers

It is straightforward to show that the characteristic time for scattering of a test star by a set of field stars having a range of masses can be written as

$$t_r = \frac{0.34\sigma^3}{G^2\tilde{m}\rho \ln \Lambda}, \quad \tilde{m} \equiv \frac{\int n(m)m^2 dm}{\int n(m)m dm} = \rho^{-1} \int n(m)m^2 dm, \quad (84)$$

where $n(m)dm$ is the number of field stars with masses in the interval dm centered on m . Equation (84) assumes that field stars of all masses have the same velocity distribution (with dispersion σ), a defensible assumption if the system is less than one relaxation time old. To a first approximation, the tidal event rates derived in the preceding sections can be generalized to a range of stellar masses by changing the mass m_\star that appears in equation (9) to \tilde{m} and computing the loss rate independently for stars in each $\{m_\star, R_\star\}$ group.

In a stellar population with a “normal” initial mass function (IMF) and in which the most massive stars have evolved off the main sequence, $\tilde{m} \approx M_\odot/2$. If a nucleus is

young enough that most of its stars are still on the main sequence, the value of \tilde{m} can be much larger. For instance, a Salpeter [52] IMF with $10^{-2}M_{\odot} \leq m \leq 10^2 M_{\odot}$ yields $\tilde{m} \approx 10^1 M_{\odot}$, corresponding to a relaxation time that is roughly ten times shorter than in an evolved cluster with the same mass density.

Consider as an extreme case a mass function consisting of stars and some set of “massive perturbers” with individual masses much greater than those of stars. We can write

$$n(m) = [n(m)]_{\text{star}} + [n(m)]_{\text{MP}} \quad (85)$$

and

$$\rho \tilde{m} = \left[\int n(m)m^2 dm \right]_{\text{star}} + \left[\int n(m)m^2 dm \right]_{\text{MP}} \quad (86a)$$

$$= \rho_{\text{star}} \tilde{m}_{\text{star}} + \rho_{\text{MP}} \tilde{m}_{\text{MP}}. \quad (86b)$$

The condition that the scattering time be determined by the massive objects is

$$(\rho \tilde{m})_{\text{MP}} \gg (\rho \tilde{m})_{\text{star}}. \quad (87)$$

Near the center of a galaxy, massive perturbers can include gas clouds with masses up to and including those of giant molecular clouds (GMCs), and star clusters, both open and globular. While mean number densities are very small—roughly 10^{-5} pc^{-3} in the case of GMCs—these objects are so much more massive than stars that they can easily dominate the gravitational scattering inside any region large enough to contain them. The dominant contribution to $\rho \tilde{m}$ turns out to come from the GMCs; in the region $1.5 \text{ pc} \lesssim r \lesssim 5 \text{ pc}$, one finds [46]

$$(\rho \tilde{m})_{\text{GMC}} \approx (20\text{--}2000) (\rho \tilde{m})_{\text{star}}. \quad (88)$$

In order to estimate the effective reduction in the timescale for gravitational scattering, we need also to take into account the large physical size of GMCs, which implies a lower effectiveness of close encounters. The Coulomb logarithm can be written as $\ln \Lambda \approx \frac{1}{2} \ln(1 + p_{\text{max}}^2/p_0^2)$. Numerical experiments [57] suggest that p_{max} is roughly 1/4 times the linear extent of the test star’s orbit. Setting this size to 10 pc, and replacing p_0 by $R \approx 5 \text{ pc}$ (1/2 the physical size of a GMC), one finds that $\ln \Lambda$ near the center of the Milky Way decreases from ~ 15 in the case of star–star scattering to ~ 0.5 in the case of scattering by GMCs. Combined with equation (88), this result suggests that the effective timescale for gravitational scattering near the Galactic center might be reduced by a factor of $\sim 10^0$ to $\sim 10^2$ due to the presence of GMCs.

What would be the consequences of such a reduction? The effect on the distribution of stars inside the influence radius of Sgr A*, $r < r_{\text{h}} \approx 2\text{--}3 \text{ pc}$, is likely to be small: at these radii, velocity perturbations are due mostly to objects within $\sim r_{\text{h}}$, a region that is not likely to contain a single massive perturber. But the supply of stars to the SBH is dominated by gravitational encounters that take place at larger radii. In the absence of massive perturbers, the transition from empty- to full-loss-cone regimes takes place roughly at $r \approx r_{\text{h}}$ in a nuclear star cluster like that of the Milky Way (figure 3). Massive

perturbers cannot increase the flux in the full-loss-cone regime, but they could convert an empty loss cone into a full loss cone, implying an increased rate of capture by the SBH.

Equation (30a) gives for the energy-dependent loss-cone flux is given in the two regimes as

$$F \approx F^{\text{flc}} \times \begin{cases} q |\ln \mathcal{R}_{\text{lc}}|^{-1}, & \text{if } q \ll -\ln \mathcal{R}_{\text{lc}}, \\ 1, & \text{if } q \gg -\ln \mathcal{R}_{\text{lc}} \end{cases}, \quad (89)$$

where F^{flc} is the full-loss-cone flux, $\mathcal{R}_{\text{lc}} \approx r_{\text{lc}}/r$, and $q \approx P/(T_r \mathcal{R}_{\text{lc}})$ with P the orbital period. A decrease in the effective value of t_r due to massive perturbers would imply a larger q , hence a smaller radius of transition to the full-loss-cone regime. But the effect on the net rate of stellar captures is likely to be modest, at least in a galaxy like the Milky Way, since the transition radius even in the absence of massive perturbers is $r_{\text{crit}} \approx r_{\text{h}}$, and since massive perturbers will not significantly decrease the effective value of t_r inside r_{h} .

These arguments are modified somewhat in the case of the interaction of *binary* stars with an SBH. The distance from an SBH at which a binary star is tidally separated, $r_{\text{t,bin}}$, is larger than the tidal disruption radius for a single star, r_{t} , by a factor

$$\frac{r_{\text{t,bin}}}{r_{\text{t}}} \approx \frac{a_{\text{bin}}}{R_{\star}} \approx 21 \left(\frac{a_{\text{bin}}}{0.1 \text{ AU}} \right) \left(\frac{R_{\star}}{R_{\odot}} \right)^{-1} \quad (90)$$

where a_{bin} is the binary semimajor axis. Identifying $r_{\text{t,bin}}$ with r_{lc} allows us to define a “capture sphere” for binary stars; the rate of diffusion of binaries into this sphere determines the rate at which, for instance, hypervelocity stars are produced [21]. Since the capture sphere for binaries is so much larger than r_{t} , the empty-loss-cone regime extends much farther out, and any mechanism that decreases the effective relaxation time can therefore have a substantial effect on the binary disruption rate. It has been argued that massive perturbers increase the rate of interaction of binary stars with the Milky Way SBH by a factor of 10^1 – 10^3 , with corresponding increases in the rate of production of hypervelocity stars, and the rate of deposition of stars in tightly bound orbits near the SBH [46].

5. Relativistic loss cones

So far only the lowest-order (1PN) relativistic corrections to the equations of motion have been considered. Higher-order PN terms, representing the effects of frame dragging, of torques due to the SBH’s quadrupole moment, etc. can also be included in the orbital equations [34]; of course, these higher-order corrections become progressively more important at smaller distances from the SBH. But sufficiently close to the SBH, the number of stars enclosed within any orbit is so small that it may no longer make sense to represent the gravitational potential from the stars as a smooth, symmetric function of position. Instead, the nonsphericity of the potential may be due mostly to the fact that at any moment, there are different numbers of stars on one side of

the SBH as compared with another. The idea is that—at least for some span of time—orbits near the SBH are nearly Keplerian, and maintain their orbital elements, including particularly their orientations. The magnitude of the torque acting on a test star in this regime is roughly

$$|\mathcal{T}| \approx \sqrt{N} \frac{Gm_\star}{a}, \quad (91)$$

where N is the number of (field) stars inside the test-star’s orbit, whose semimajor axis is a , and m_\star is the mass of one field star. Furthermore, since orbital periods P are generally much smaller than the time for orbital elements to change, it is reasonable to compute the torques by averaging each orbit with respect to mean anomaly; in effect, replacing each star by an elliptical ring of mass.⁺

This “ \sqrt{N} torque” will dominate the torque from the large-scale nuclear nonsphericity if

$$N(a) \lesssim \epsilon^{-2} \quad (92)$$

with ϵ defined in equation (40). So, for instance, if the nucleus is modestly elongated, $\epsilon \sim 10^{-1}$, then at radii where $N(< a) \lesssim 10^2$, the \sqrt{N} torques will dominate torques from the large-scale distortion. In the Milky Way, the corresponding radius might be $\sim 10^{-3} - 10^{-2}$ pc depending on the poorly-known distribution of stars and stellar remnants at these radii [24, 32]. One can obtain an approximate understanding of the motion in this regime by supposing that the \sqrt{N} torques are representable approximately in terms of an axisymmetric or triaxial distortion (say), with amplitude given by $\epsilon \approx 1/\sqrt{N}$, and applying the results derived above. What makes the problem much more interesting, and difficult, is the fact that the orbits generating the torque do not maintain their orientations forever: they precess, causing the direction of the torque generated by them to change with time in some complicated way.

Evolution of orbits in response to \sqrt{N} torques is called “resonant relaxation” (RR) [49]. On time scales short compared with typical precession times, such evolution is “coherent”: the angular momentum of a test star increases approximately linearly with time in response to the nearly-constant torques. On longer time scales, the direction of the \sqrt{N} torques is changing, and the response of a single orbit to the torques will be more like a random walk; this is the “incoherent” regime. The torques also affect the precession *rates*, but only slightly, and to a good approximation, the rate at which stars precess can be computed by assuming that the stellar potential is spherical.

But at these small distances from the SBH, apsidal precession due to relativity typically can not be ignored, and it affects the motion in two important ways.* (i) *Individual* stars on eccentric orbits can come close enough to the SBH that they experience relativistic precession in a time short compared with the time for a typical star

⁺ A similar averaging technique is the basis for the derivation of the orbit-averaged Fokker-Planck equation (section 2.2); the Kozai-Lidov oscillations; and the results presented in sections 3.1–3.2 for motion in axisymmetric and triaxial potentials, among many other examples in the literature.

* Other effects of relativity, including spin-orbit torques and gravitational-wave energy loss, are considered below.

of the same a to precess. This is similar to the behavior of a star on a saucer or pyramid orbit as it nears the point of maximum eccentricity allowed by GR, as discussed above, and one expects that the rate at which such a star random-walks in angular momentum space (due to “incoherent RR”) will drop precipitously when GR precession is so rapid as to “quench” the effects of the \sqrt{N} torques [39]. (ii) Sufficiently close to the SBH, *most* stars will precess in response to GR at a faster rate than precession due to other sources (e.g. mass precession). When this condition is met, GR sets the “coherence time,” the time over which the \sqrt{N} torques are nearly constant [49].

Taking the second of these first, we can define the coherence time, t_{coh} , at radius a as the time for an orbit of typical eccentricity to precess by an angle $\sim \pi$. If precession is dominated by GR then equation (44) gives

$$t_{\text{coh,S}}(a) \approx \frac{1}{12} \frac{a}{r_g} P(a) \quad (93)$$

while if mass precession is dominant,

$$t_{\text{coh,M}}(a) \approx \frac{M_\bullet}{N(a)m_\star} P(a). \quad (94)$$

The coherence time is set by the shorter of these; $t_{\text{coh,S}}$ is shorter than $t_{\text{coh,M}}$ when

$$aN(a) \lesssim 12 \frac{M_\bullet}{m_\star} r_g. \quad (95)$$

In the Milky Way, the radius separating the two regimes is probably $\sim 10^{-2} - 10^{-1}$ pc.

As long as the “test” star is not precessing much faster than the “field” stars, it feels a nearly constant torque over $\Delta t \lesssim t_{\text{coh}}$, causing its angular momentum to change by

$$|\Delta L|_{\text{coh}} \approx |\mathcal{T}| \Delta t \approx \sqrt{N} \frac{Gm_\star}{a} \Delta t, \quad \Delta t \lesssim t_{\text{coh}}. \quad (96)$$

On time scales longer than t_{coh} , the \sqrt{N} torques from the field stars are changing direction in some complicated way, and $|\Delta L|_{\text{coh}}$ sets the step-length for a random walk:

$$|\Delta \mathbf{L}| \approx |\Delta \mathbf{L}|_{\text{coh,s}} \left(\frac{\Delta t}{t_{\text{coh}}} \right)^{1/2}, \quad \Delta t \gtrsim t_{\text{coh}}. \quad (97)$$

We can write this as

$$\frac{|\Delta \mathbf{L}|}{L_c} = \left(\frac{\Delta t}{t_{\text{RR}}} \right)^{1/2}, \quad t_{\text{RR}} \equiv \left(\frac{L_c}{|\Delta \mathbf{L}|_{\text{coh}}} \right)^2 t_{\text{coh}} \quad (98)$$

with t_{RR} the (incoherent) “resonant-relaxation time”:

$$t_{\text{RR}} \approx \begin{cases} \left(\frac{M_\bullet}{m} \right) P, & t_{\text{coh}} = t_{\text{coh,M}} \\ \frac{3}{\pi^2} \frac{r_g}{a} \left(\frac{M_\bullet}{m} \right)^2 \frac{P}{N}, & t_{\text{coh}} = t_{\text{coh,S}}. \end{cases} \quad (99)$$

These times can be compared to the time associated with non-resonant relaxation (NRR), equation (9), which can be rewritten approximately as[‡]

$$t_{\text{NRR}} \approx \frac{C_{\text{NRR}}}{\ln \Lambda} \left(\frac{M_{\bullet}}{m} \right)^2 \frac{P}{N}, \quad C_{\text{NRR}} \approx 0.1. \quad (100)$$

The condition $t_{\text{RR}} < t_{\text{NRR}}$ becomes

$$m_{\star} N(r < a) \lesssim \frac{M_{\bullet}}{\ln \Lambda}, \quad t_{\text{coh}} = t_{\text{coh},\text{M}} \quad (101a)$$

$$N(r < a) \lesssim C_{\text{NRR}}^{1/2} \left(\frac{a}{r_{\text{g}}} \right)^{1/2}, \quad t_{\text{coh}} = t_{\text{coh},\text{S}}. \quad (101b)$$

At the Galactic center, the critical radius at which $t_{\text{RR}} \approx t_{\text{NRR}}$ is ~ 0.05 pc if there is a steeply-rising density of stars and stellar remnants near the SBH [24]; or ~ 0.2 pc if the mass distribution is assumed to follow what is observed in the bright, late-type stars, i.e. a central “core” [32]. These radii are small compared with the radius at which most normal stars would be scattered into the SBH, whether by gravitational encounters, or by torques from the large-scale mass distribution, and for this reason, resonant relaxation is typically assumed not to strongly affect the event rates.

But the situation can be very different in the case of compact remnants. These include stellar-mass black holes (BHs) and neutron stars, the end-states of the evolution of stars more massive than about $8M_{\odot}$. The characteristic distance from which compact remnants would be scattered into a SBH is smaller than for ordinary stars, for two reasons: remnants can survive tidal disruption to much smaller separations; and—in the case of stellar-mass BHs, which have masses $\sim 5M_{\odot} - 20M_{\odot}$ —mass segregation can cause them to accumulate near the SBH. The latter mechanism occurs on a time scale of $\sim (m_{\star}/m_{\bullet})t_{\text{NRR}}$, where m_{\bullet} is the BH mass. This time may be less than 10 Gyr at the Galactic center, and in “relaxed” models of the stellar distribution, the number (mass) density of BHs exceeds that of main-sequence stars at a distance of $\sim 10^{-2}$ ($\sim 10^{-3}$) pc from the Milky Way SBH [24]. However these models do not correctly reproduce the observed distribution of normal stars (i.e. red giants), which exhibit a low-density core near the SBH [7, 12, 4], suggesting that the relaxation time in the Galactic center may not be short enough for a steady-state distribution to have been reached [32].

But suppose that the density in *some* nucleus (perhaps a nucleus containing a SBH less massive than the Milky Way’s) is dominated by stellar remnants at radii $\ll r_{\text{h}}$, and that the resonant relaxation time (the time for changing orbital angular momenta) is much shorter, at these radii, than the non-resonant relaxation time (the time for changing orbital energies). Orbits of the remnants will undergo a random walk in \mathbf{L} with characteristic time t_{RR} ; since orbital energies remain nearly constant, changes in L correspond to changes in eccentricity e and hence to changes in the radius of periapsis, $r_{\text{peri}} = a(1 - e)$. In order to be captured by the SBH, one of two things must happen. (i) r_{peri} falls below a few r_{g} ; e.g. for a non-spinning hole capture occurs if $r_{\text{peri}} \lesssim 8r_{\text{g}}$

[‡] Note that t_{NRR} is the same quantity as t_r defined above.

[63]. Since $a \gg r_g$, the eccentricity of such a capture orbit would be extremely high, $10^{-5} \lesssim 1 - e \lesssim 10^{-3}$, much higher than the average value $\langle e \rangle = 2/3$ for a “thermal” distribution of orbits around a point mass. (ii) The time scale for energy loss due to gravitational wave (GW) emission falls below the time for orbital angular momenta to change, e.g., $(1 - e)t_{\text{RR}}$. GW energy loss causes the semimajor axis of the orbit to shrink, initially at roughly constant r_{peri} [47], until the orbit becomes nearly circular and the BH spirals into the SBH. The former channel is called a “plunge” and the latter an “EMRI,” or extreme-mass-ratio inspiral [1, 56].

The model as just described predicts interestingly high rates of capture [23], but there is a problem. As noted above, individual orbits that are highly eccentric will precess due to GR at a rate much higher than the rates of precession of other stars with the same a . In fact an eccentric orbit can precess so rapidly that the net effect of the \sqrt{N} torques, over one GR precessional cycle, is very small. An equivalent way to say this is that—for a very eccentric orbit—the effective time over which the background torques can act coherently is given by *its* precession time, and not by the average (and much longer) precession time, t_{coh} , of the other orbits.

The residual torque produced by an otherwise-spherical distribution of stars is given by equation (91). Writing $L = [GM_{\bullet}a(1 - e^2)]^{1/2}$ for the angular momentum of a test orbit, the time scale over which the (fixed) torque changes L is

$$\left| \frac{1}{L} \frac{dL}{dt} \right|^{-1} \approx \sqrt{N(a)} \frac{M_{\bullet}}{M_{\star}(a)} \left[\frac{a^3(1 - e^2)}{GM_{\bullet}} \right]^{1/2}. \quad (102)$$

(Note that we are comparing changes in L to its own value, and not to L_c .) The condition that this time be shorter than the relativistic precession time is^{††}

$$\sqrt{1 - e^2} \gtrsim \frac{r_g M_{\bullet}}{a m_{\star}} \frac{1}{\sqrt{N(a)}}. \quad (103)$$

The same functional relation between a and e can be derived, up to a factor of order unity, from expressions like (48), the minimum angular momentum attainable by a saucer or pyramid orbit in a fixed nonspherical potential, after replacing ϵ by $1/\sqrt{N}$ [39].

The curve (103) is plotted as the dotted lines on figure 14, which is taken from the N -body study in which the phenomenon was discovered [35]. The N -body results confirm that stars are reluctant to cross this “Schwarzschild barrier” (SB), which defines a locus of maximum eccentricity in the (a, e) plane. The barrier is predicted to exist for orbits with semimajor axes between a_{min} and a_{max} : the first value is obtained by setting $e = 0$ in equation (103), the second by the intersection of that relation with the capture line, $r_{\text{peri}} = a(1 - e) = \Theta r_g \approx 8r_g$. These limits can be expressed approximately as

$$\left(\frac{a_{\text{min}}}{\text{mpc}} \right)^2 \left(\frac{N_{\text{min}}}{10^2} \right) \approx 0.2 \left(\frac{M_{\bullet}}{10^6 M_{\odot}} \right)^4 \left(\frac{m_{\star}}{10 M_{\odot}} \right)^{-2},$$

^{††}Due to a typesetter’s error, the expression given for Eq. 103 in [33], equation 6.195, is missing the square root on the left hand side.

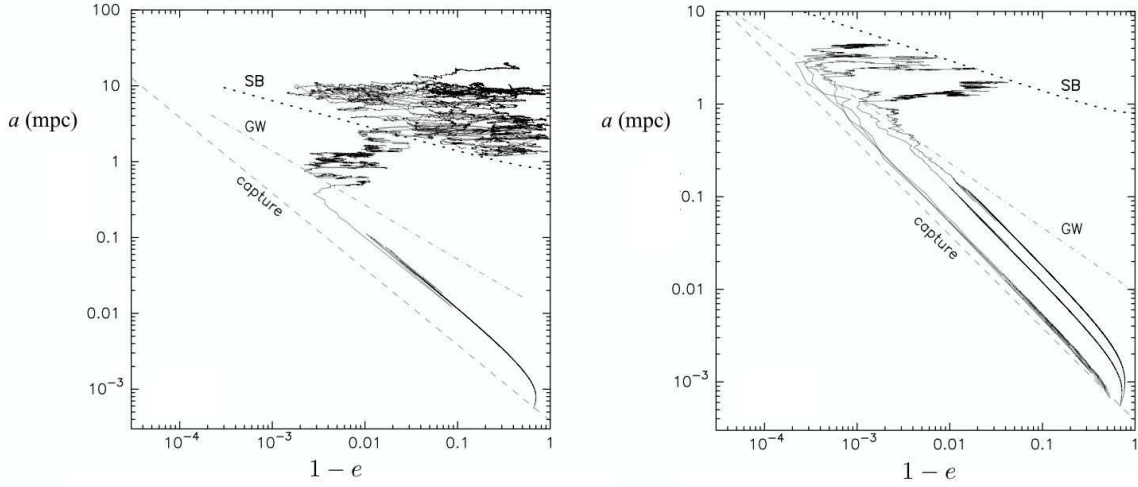


Figure 14. Relativistic N -body simulation of EMRI formation [35]. The left panel shows the trajectories, over a time interval of 2 Myr, of stellar-mass black holes orbiting a $10^6 M_\odot$ SBH as they undergo gravitational encounters with each other. Motion in the (a, e) plane is mostly horizontal due to the fact that resonant relaxation causes changes in angular momentum (i.e., e) on a timescale that is much shorter than non-resonant relaxation causes changes in energy (i.e., a). The dashed line marked “capture” is the capture radius around the SBH; the dotted line marked “SB” is equation (103); and the dot-dashed line marked “GW” indicates the locus in the a - e plane where angular momentum loss due to gravitational radiation dominates changes due to gravitational encounters. Only one object in the left panel manages to cross the GW line and become an EMRI; most of the other objects are reflected by the eccentricity barrier before reaching the gravitational-wave regime. There are no “plunges.” The right-hand panel, a montage from several independent N -body integrations, shows a number of EMRI events like the single event in the left-hand panel.

$$\left(\frac{a_{\max}}{\text{mpc}}\right) \left(\frac{N_{\max}}{10^2}\right) \approx 300 \left(\frac{\Theta}{8}\right)^{-1} \left(\frac{M_\bullet}{10^6 M_\odot}\right)^3 \left(\frac{m_\star}{10 M_\odot}\right)^{-2} \quad (104)$$

where $\text{mpc} \equiv 10^{-3} \text{ pc}$ and $N_{\{\min, \max\}}$ is the number of stars (or BHs), of mass m_\star , inside radius $r = \{a_{\min}, a_{\max}\}$. If we adopt equation (31) for $\rho(r)$ —the “singular isothermal sphere”—these relations become

$$\begin{aligned} a_{\min} &\approx 0.35 \left(\frac{M_\bullet}{10^6 M_\odot}\right)^{4/3} \left(\frac{m_\star}{10 M_\odot}\right)^{-1/3} \left(\frac{\sigma}{100 \text{ kms}^{-1}}\right)^{-2/3} \text{ mpc} , \\ a_{\max} &\approx 8.0 \left(\frac{\Theta}{8}\right)^{-1/2} \left(\frac{M_\bullet}{10^6 M_\odot}\right)^{3/2} \left(\frac{m_\star}{10 M_\odot}\right)^{-1/2} \left(\frac{\sigma}{100 \text{ kms}^{-1}}\right)^{-1} \text{ mpc} \end{aligned} \quad (105)$$

or

$$\begin{aligned} a_{\min} &\approx 0.44 \left(\frac{M_\bullet}{10^6 M_\odot}\right)^{1.2} \left(\frac{m_\star}{10 M_\odot}\right)^{-1/3} \text{ mpc} , \\ a_{\max} &\approx 11 \left(\frac{\Theta}{8}\right)^{-1/2} \left(\frac{M_\bullet}{10^6 M_\odot}\right)^{1.3} \left(\frac{m_\star}{10 M_\odot}\right)^{-1/2} \text{ mpc} \end{aligned}$$

(106)

if the M_\bullet - σ relation [17] is used to eliminate σ . These scalings suggest that the relative extent of the barrier, a_{\max}/a_{\min} , is nearly independent of M_\bullet and m_\star :

$$\frac{a_{\max}}{a_{\min}} \approx 25 \left(\frac{\Theta}{8}\right)^{-1/2} \left(\frac{M_\bullet}{10^6 M_\odot}\right)^{0.1} \left(\frac{m_\star}{10 M_\odot}\right)^{-1/6}. \quad (107)$$

Note that these relations would only be expected to hold in galaxies containing nuclear star clusters; galaxies having $M_\bullet \gtrsim 10^8 M_\odot$ tend to exhibit central cores, not NSCs, as discussed above. The estimated value of a_{\max} is small compared with SBH influence radii (equation 5), and so the existence of the SB is not likely to have much consequence for the rate of tidal disruption of normal stars. But the barrier can be expected to play a critical role in mediating the capture of stellar remnants, or in determining the steady-state distribution of any other nuclear component that can resist tidal disruption (dark matter particles, planetesimals, etc.) at radii $r \lesssim a_{\max}$ [22, 64].

An orbit that “strikes the barrier” from above (i.e. from a region of lower eccentricity) might be expected to behave—for a time less than $\sim t_{\text{coh}}$ —in a manner similar to orbits in fixed, axisymmetric or triaxial potentials when their angular momenta reach values close to the minimum allowed by GR precession (e.g. equation 48; figure 8). In other words: L should oscillate near its minimum value, at roughly the GR precessional frequency. That is roughly what is observed to happen in the N -body experiments [35]; but after remaining near the barrier for a few GR precessional periods, orbits are observed to “bounce back” to lower values of e , where RR is once again effective. What makes the behavior of orbits in an N -body system more complex than in a fixed potential is, of course, that the potential generating the \sqrt{N} torques is not constant: the field star orbits also precess, and after a time $\sim t_{\text{coh}}$, the direction of the torques (and to a lesser extent, their magnitude) will have changed in some complex, but essentially random, way.

Near and below the barrier, orbits precess with frequency $\sim |d\omega/dt|_S$ (equation 44). Precession in the nearly fixed \sqrt{N} potential results in a periodic variation in the test star’s angular momentum $\ell \equiv L/L_c = \sqrt{1 - e^2}$:

$$\ell(t) \approx \langle \ell \rangle [1 - C \times \langle \ell \rangle \cos(\nu t)], \quad \nu = \frac{3(GM_\bullet)^{3/2}}{c^2 a^{5/2} \langle \ell \rangle^2} \quad (108)$$

where $C = C(a)$ is a poorly-determined “constant” of order

$$C \approx \frac{\sqrt{N} m_\star a}{2 M_\bullet r_g}. \quad (109)$$

The amplitude of these oscillations is $\ell_+ - \ell_- \approx 2C\langle \ell \rangle^2$; below the SB, the amplitude drops rapidly, as $\sim (1 - e^2)$. On time scales *longer* than t_{coh} , one might expect that changes in the direction and amplitude of the \sqrt{N} torques would add a random component to the otherwise periodic variations in ℓ [35]. As of this writing, there does not exist a good theoretical description of how orbits evolve in this regime: that is: in response to (time-dependent) \sqrt{N} torques below the SB. However, Monte-Carlo

simulations, based on a simple (perhaps too simple) Hamiltonian model [35], suggest that $\langle \ell \rangle$ would indeed undergo a random walk in this regime. Since this evolution is not well described either as “resonant relaxation” (RR) or “non-resonant relaxation” (NRR), a new name seems appropriate. Here we will call it “anomalous relaxation” (AR).

One reason it is difficult to study AR via N -body simulations is that its effects tend to be obscured by those of NRR, and to a greater degree than would be expected in real nuclei. Even though $t_{\text{RR}} \ll t_{\text{NRR}}$ at these radii, it does not follow that NRR can be ignored near or below the barrier, since the effects of the \sqrt{N} torques are so strongly suppressed by the rapid GR precession. In fact at any $a \in [a_{\text{min}}, a_{\text{max}}]$, there will be some eccentricity above which changes in angular momentum due to NRR are larger than those due to the \sqrt{N} torques. The time to change L by of order itself due to NRR is

$$t_1 \approx \ell^2 t_{\text{NRR}}(a) \approx 0.2(1-e) \left(\frac{M_\bullet}{m} \right)^2 \frac{P}{N \ln \Lambda} \quad (110)$$

(equation 100). Let t_2 be the time for changes in L due to AR, that is, due to the \sqrt{N} torques alone, in the regime below the SB where GR precession is rapid. While the L -dependence of t_2 is currently unknown, one expects t_2 to be an increasing function of e , since the increasingly rapid GR precession below the barrier implies an increasing degree of adiabatic invariance of the orbit’s elements, and this expectation is at least qualitatively consistent with results from the crude Hamiltonian model mentioned above. One estimate of the ratio of the two times, along the SB, is [35]

$$\begin{aligned} \left. \frac{t_1}{t_2} \right|_{\text{SB}} &\approx \frac{1}{4C^2} \frac{t_{\text{NRR}}}{t_{\text{coh}}} \approx \frac{1}{N(a)} \left(\frac{M_\bullet}{m_\star} \right)^2 \left(\frac{r_g}{a} \right)^2 \frac{t_{\text{NRR}}(a)}{t_{\text{coh}}(a)} \\ &\approx \frac{0.1}{\ln \Lambda} \left[\frac{M_\bullet}{M_\star(a)} \right]^3 N^2(a) \left(\frac{r_g}{a} \right)^2, \quad a \in [a_{\text{min}}, a_{\text{max}}] \end{aligned} \quad (111)$$

where the latter expression sets $t_{\text{coh}} = t_{\text{coh},M}$. This scaling (if correct) suggests that $t_1/t_2 \propto N^2$ in a nuclear model of specified M_\bullet and mass density. Since the N -body simulations [35, 5] have so far adopted unrealistically small values of N (i.e. too-large values of m_\star), one expects that they have been affected by NRR to a greater degree than in real nuclei, and hence that the simulated rates of capture were too high. Before reliable estimates of capture rates can be made, simulations with substantially larger N will need to be carried out. This is an extremely demanding problem from a computational point of view, and a significant increase in the efficiency of N -body algorithms will probably be needed in order to achieve this.

Another important question that will require large- N simulations is the steady-state distribution of stars or stellar remnants, with respect to angular momentum, near the SB. Imagine starting from a nucleus in which the region below the barrier is unpopulated; ignore the effects of GW energy loss (appropriate if the test bodies are of sufficiently low mass). From time to time, penetration of the barrier from above will place a star below, where it will remain for a long time, since the time scale for changes in L below

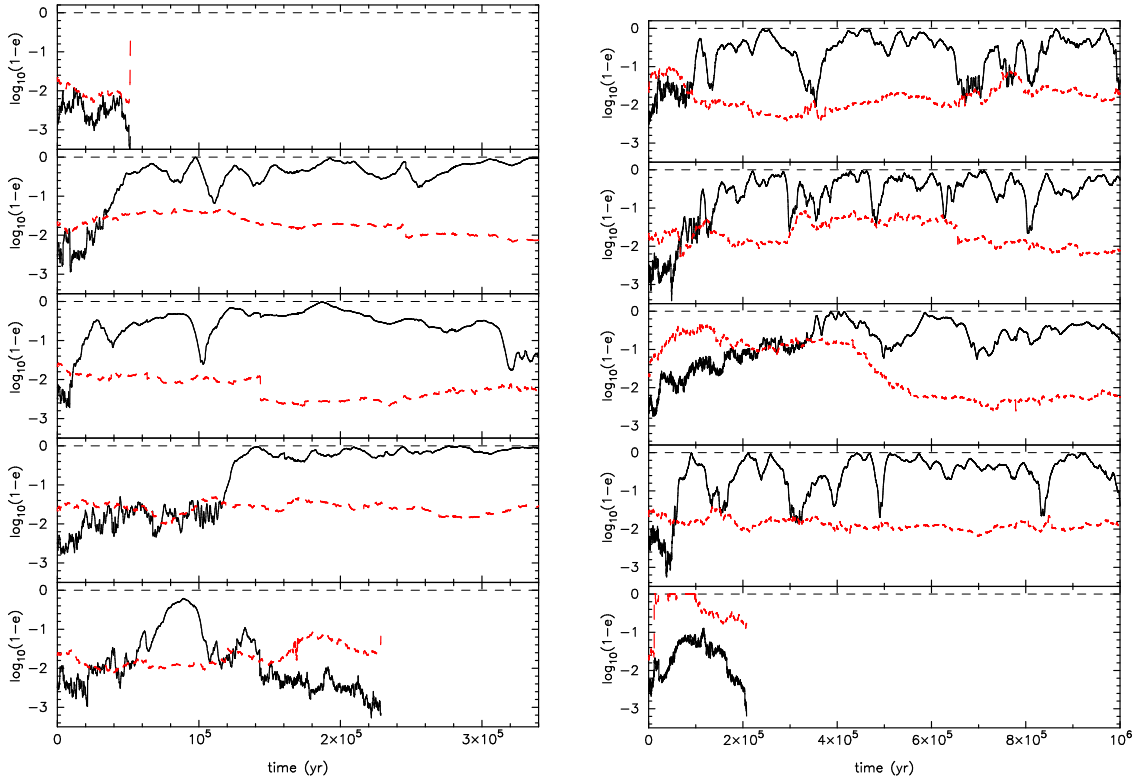


Figure 15. Eccentricity evolution of stars started “below” the Schwarzschild barrier (SB) in a relativistic N -body integration, including (left) and without (right) the 2.5PN terms. Solid (black) lines show $\log(1 - e)$ and dotted (red) lines show the predicted eccentricity of the SB, equation (103); the latter changes with time due to changes in the stars semi-major axis a . The lines terminate when the star is captured by the SBH, which occurs in three of the panels. Note two phenomena associated with the SB: the “bounce” that occurs when a star strikes the barrier from above; and the “buoyancy” exhibited by a star that crosses the barrier from below.

the barrier is long compared with the RR time (figure 15). Eventually, the number of stars below the barrier will be so large that the rate of passage from below to above will equal the rate from above to below. The net rate of feeding of stars to the SBH will be set by this steady-state distribution.

While existing simulations probably do not have large enough N to derive this distribution, there are other interesting questions whose answers do not depend on knowing the steady-state $N(L)$. One such question is the origin of the S-stars, the bright, upper-main-sequence stars that are observed to populate the inner ~ 0.1 pc of the Galactic center [25]. These stars follow orbits with a nearly “thermal” distribution of eccentricities, $N(e) de \sim e de$ [20]; whereas the leading model for their origin posits that they were deposited on orbits of much higher eccentricity via exchange interactions involving pre-existing binary stars [46]. Since the ages of the S-stars are less than about 100 Myr, one needs to explain how such extremely eccentric orbits evolved to their more modest eccentricities in a relatively short time. Purely Newtonian simulations [45] suggested that RR could achieve this, at least in nuclei with a sufficiently (and probably

unphysically large) density of compact-object perturbers. But positing initially very eccentric orbits for the S-stars would almost certainly place them below the SB, and their subsequent evolution would be something like that of the test-particles shown in figure 15. After some time (which turns out to be of order 10^7 in the Galactic center), such a star may cross the SB from below to above, at which point RR “turns on” and carries it to much higher angular momenta (lower e) in a time $\sim t_{\text{RR}}$. This “buoyancy” effect can clearly be seen in several panels of figure 15 and it is a plausible explanation for the current $N(e)$ distribution of the S-stars [2]. While this is not strictly speaking a loss-cone problem, it does show that the SB can be important for the evolution of the orbits of normal stars, even stars that are directly observed.

Efforts are currently underway to build instruments capable of carrying out infrared astrometry to 10 micro-arc-second accuracy for stars near the Milky Way SBH [14]; one goal is to observe deviations from Keplerian motion over time spans of a few years in the orbits of stars with semimajor axes somewhat smaller than that of S2. For these stars, the major sources of evolution are likely to be relativistic (Schwarzschild) precession of the periapsis, equation (44), and mass precession, equation (67). In addition, the \sqrt{N} torques will induce changes in all the other Kepler elements, at the rate defined above for “coherent resonant relaxation,” equation (96). So, for instance, the changes over one orbital period of the eccentricity, Δe , and the direction of the orbital angular momentum vector, $\Delta\theta$, would be given by relations like

$$|\Delta e| \approx C_e \sqrt{N} \frac{m_\star}{M_\bullet}, \quad (112a)$$

$$\Delta\theta \approx 2\pi C_t \sqrt{N} \frac{m_\star}{M_\bullet}, \quad (112b)$$

where N is understood to be the average number of stars inside the apoapsis of the orbit. Numerical experiments [51] confirm these predictions and allow the coefficients $\{C_e, C_t\}$ to be calibrated. Because the changes in the star’s orbit due to the \sqrt{N} torques scale differently with m_\star and N than the changes due to the smoothly-distributed mass ($\propto M_\star = Nm_\star$), both the number and mass of the perturbing objects within the observed star’s orbit can in principle be independently constrained [51]. For instance, one could determine M_\star by comparing the observed apsidal precession with the relativistic contribution (44), then compute $m_\star\sqrt{N}$ by measuring changes in e or θ and comparing with equations (112a)-(112b).

The relativistic effects described so far are a consequence of the lowest-order (1PN) corrections to the Newtonian equations of motion. What about the higher-order terms? Energy loss due to GW emission is first reproduced at 2.5PN order, and in fact the simulations shown in figures 14 and 15 included the 2.5PN terms [35]. If the SBH is spinning (as it almost certainly is), there are additional corrections to the test-mass equations of motion at low PN order. These spin-orbit (Lense-Thirring, Kerr) terms imply an additional degree of apsidal precession of an orbiting star; this precession can usually be ignored compared with the Schwarzschild precession. But the torques from a spinning hole also have a component which causes the orbital line of nodes, Ω , to

precess, thereby changing the direction of the orbital angular momentum vector \mathbf{L} . The (orbit-averaged) rates of precession of a test mass's orbit due to the SBH spin are given by

$$\left\langle \frac{d\Omega}{dt} \right\rangle_{\text{K}} = \frac{2G^2 M_{\bullet}^2 \chi}{c^3 a^3 (1-e^2)^{3/2}} = \frac{2GS}{c^2 a^3 (1-e^2)^{3/2}}, \quad (113a)$$

$$\left\langle \frac{d\omega}{dt} \right\rangle_{\text{K}} = -\frac{6G^2 M_{\bullet}^2 \chi}{c^3 a^3 (1-e^2)^{3/2}} \cos i = -\frac{6GS}{c^2 a^3 (1-e^2)^{3/2}} \cos i \quad (113b)$$

where $\chi \equiv cS/(GM_{\bullet})$ is the dimensionless spin, i is the inclination of the star's orbit with respect to the SBH's equatorial plane, and Ω is defined also with respect to that plane.

Just as there is a locus in the (a, e) plane where Schwarzschild (apsidal) precession inhibits the ability of the \sqrt{N} torques to change the magnitude of \mathbf{L} (equation 103), so is there another curve along which Kerr (nodal) precession inhibits the ability of the \sqrt{N} torques to change the *direction* of \mathbf{L} . The latter is given roughly by

$$(1-e^2)^3 \left(\frac{a}{r_g} \right)^3 \approx \frac{16\chi^2}{N(a)} \left(\frac{M_{\bullet}}{m_{\star}} \right)^2, \quad (114)$$

which for a power-law ($\rho \propto r^{-\gamma}$) distribution of field stars can be written

$$(1-e^2)^3 \left(\frac{a}{a_K} \right)^{6-\gamma} \approx 1, \quad (115a)$$

$$a_K = r_g \left(8\chi^2 \frac{M_{\bullet}}{m_{\star}} \right)^{1/(6-\gamma)} \left(\frac{r_m}{r_g} \right)^{(3-\gamma)/(6-\gamma)} \quad (115b)$$

where a_K is the “rotational influence radius” of the SBH [40]. For reasonable nuclear models, this radius is, very roughly, $a_K \approx 10^4 r_g$: small compared with the radii $\{a_{\min}, a_{\max}\}$ that define the SB, but large compared with the capture radius around the SBH. At $r \lesssim a_K$, orbits evolve “collisionlessly” in response to the Lense-Thirring torques, while for $r \gtrsim a_K$, star-star interactions cause orbital planes to undergo a random walk on the (coherent) RR time scale (figure 16). Note that there is no “barrier” associated with the rotational torques because at these small radii the \sqrt{N} torques are essentially unable to change orbital eccentricities due to the rapid apsidal precession. Nevertheless, to the extent that the capture condition for a spinning SBH is dependent on orbital orientations, the transition from orderly precession at $r \lesssim a_K$ to a random walk of the orbital elements at $a \gtrsim a_K$ undoubtedly has consequences for the loss-cone problem, which however have yet to be worked out.

Acknowledgments

This work was supported by the National Science Foundation under grant no. AST 1211602 and by the National Aeronautics and Space Administration under grant no. NNX13AG92G. Much of the work described here, including some unpublished work, was carried out in collaboration with F. Antonini, A. Hamers, S. Mikkola, S. Portegies

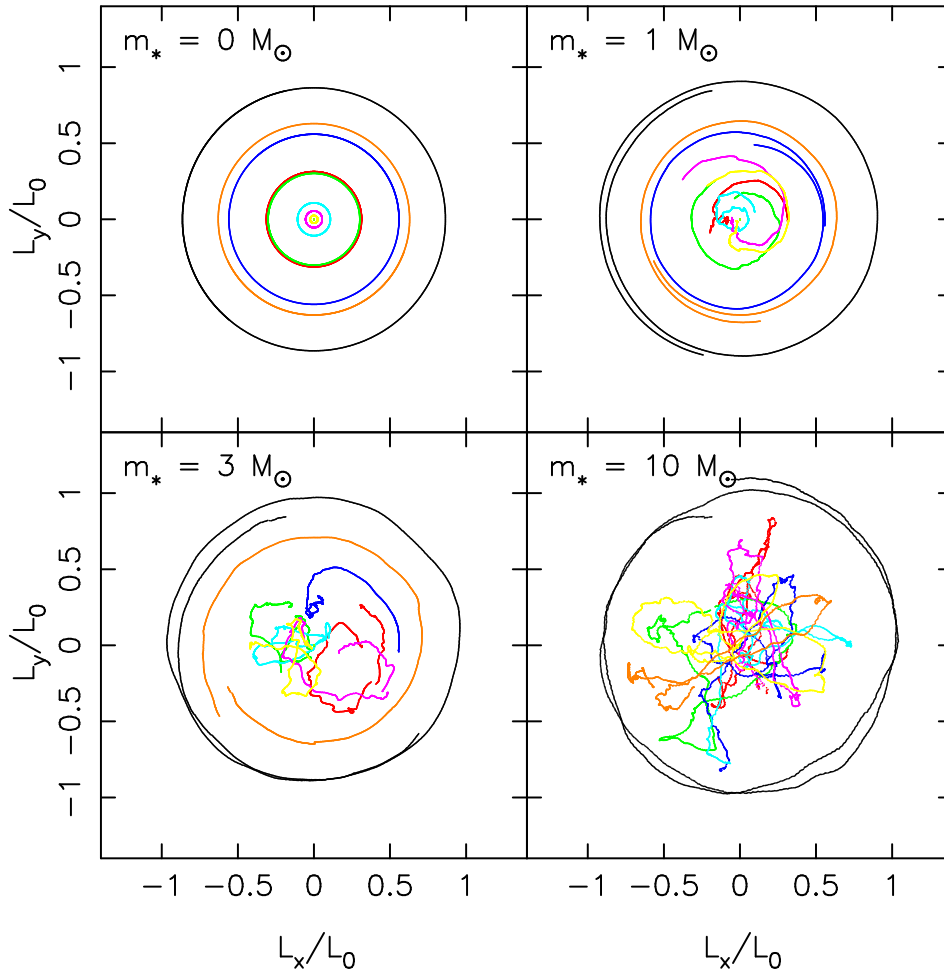


Figure 16. Evolution of orbital planes in an N -body simulation of a cluster of eight stars orbiting about the Galactic center SBH ($M_{\bullet} = 4 \times 10^6 M_{\odot}$) for an elapsed time of 2×10^6 yr [34]. The SBH rotates about the z -axis with maximal spin. Four different values were assumed for the stellar masses m_* , as indicated. Stars were placed initially on orbits with semimajor axis $a = 2$ mpc and eccentricity 0.5 and with random orientations. In a nucleus containing stars of a given mass, the transition between motion like that in the first and last panels occurs at the “rotational influence radius” (114).

Zwart, E. Vasiliev, C. Will, and particularly with T. Alexander. I thank E. V. for supplying figure 7. I thank the referees, H. Perets and D. Pfenniger, for comments which improved the presentation.

References

- [1] P. Amaro-Seoane, J. R. Gair, M. Freitag, M. C. Miller, I. Mandel, C. J. Cutler, and S. Babak. TOPICAL REVIEW: Intermediate and extreme mass-ratio inspirals: astrophysics, science applications and detection using LISA. *Classical and Quantum Gravity*, 24:113, September 2007.

- [2] F. Antonini and D. Merritt. Relativity and the Evolution of the Galactic Center S-star orbits. *Astrophys. J. Letts.*, 763:L10, January 2013.
- [3] J. N. Bahcall and R. A. Wolf. Star distribution around a massive black hole in a globular cluster. *Astrophys. J.*, 209:214–232, October 1976.
- [4] H. Bartko, F. Martins, S. Trippe, T. K. Fritz, R. Genzel, T. Ott, F. Eisenhauer, S. Gillessen, T. Paumard, T. Alexander, K. Dodds-Eden, O. Gerhard, Y. Levin, L. Mascetti, S. Nayakshin, H. B. Perets, G. Perrin, O. Pfuhl, M. J. Reid, D. Rouan, M. Zilka, and A. Sternberg. An Extremely Top-Heavy Initial Mass Function in the Galactic Center Stellar Disks. *Astrophys. J.*, 708:834–840, January 2010.
- [5] P. Brem, P. Amaro-Seoane, and C. F. Sopuerta. Blocking low-eccentricity EMRIs: A statistical direct-summation N-body study of the Schwarzschild barrier. *ArXiv e-prints*, November 2013.
- [6] M. Brockamp, H. Baumgardt, and P. Kroupa. Tidal disruption rate of stars by supermassive black holes obtained by direct N-body simulations. *Mon. Not. R. Astron. Soc.*, 418:1308–1324, December 2011.
- [7] R. M. Buchholz, R. Schödel, and A. Eckart. Composition of the galactic center star cluster. Population analysis from adaptive optics narrow band spectral energy distributions. *Astron. Astrophys.*, 499:483–501, May 2009.
- [8] S. Chandrasekhar. *Ellipsoidal figures of equilibrium*. Yale University Press, 1969.
- [9] H. Cohn and R. M. Kulsrud. The stellar distribution around a black hole - Numerical integration of the Fokker-Planck equation. *Astrophys. J.*, 226:1087–1108, December 1978.
- [10] P. Côté, S. Piatek, L. Ferrarese, A. Jordán, D. Merritt, E. W. Peng, M. Häşegan, J. P. Blakeslee, S. Mei, M. J. West, M. Milosavljević, and J. L. Tonry. The ACS Virgo Cluster Survey. VIII. The Nuclei of Early-Type Galaxies. *Astrophys. J. Suppl.*, 165:57–94, July 2006.
- [11] P. Diener, A. G. Kosovichev, E. V. Kotok, I. D. Novikov, and C. J. Pethick. Non-linear effects at tidal capture of stars by a massive black hole - II. Compressible affine models and tidal interaction after capture. *Mon. Not. R. Astron. Soc.*, 275:498–506, July 1995.
- [12] T. Do, A. M. Ghez, M. R. Morris, J. R. Lu, K. Matthews, S. Yelda, and J. Larkin. High Angular Resolution Integral-Field Spectroscopy of the Galaxy’s Nuclear Cluster: A Missing Stellar Cusp? *Astrophys. J.*, 703:1323–1337, October 2010.
- [13] C. Einsel and R. Spurzem. Dynamical evolution of rotating stellar systems - I. Pre-collapse, equal-mass system. *Mon. Not. R. Astron. Soc.*, 302:81–95, January 1999.
- [14] F. Eisenhauer, G. Perrin, W. Brandner, C. Straubmeier, K. Perraut, A. Amorim, M. Schöller, S. Gillessen, P. Kervella, M. Benisty, C. Araujo-Hauck, L. Jocou, J. Lima, G. Jakob, M. Haug, Y. Clénet, T. Henning, A. Eckart, J.-P. Berger, P. Garcia, R. Abuter, S. Kellner, T. Paumard, S. Hippler, S. Fischer, T. Moulin, J. Villate, G. Avila, A. Gräter, S. Lacour, A. Huber, M. Wiest, A. Nolot, P. Carvas, R. Dorn, O. Pfuhl, E. Gendron, S. Kendrew, S. Yazici, S. Anton, Y. Jung, M. Thiel, É. Choquet, R. Klein, P. Teixeira, P. Gitton, D. Moch, F. Vincent, N. Kudryavtseva, S. Ströbele, S. Sturm, P. Fédou, R. Lenzen, P. Jolley, C. Kister, V. Lapeyrère, V. Naranjo, C. Lucuix, R. Hofmann, F. Chapron, U. Neumann, L. Mehrgan, O. Hans, G. Rousset, J. Ramos, M. Suarez, R. Lederer, J.-M. Reess, R.-R. Rohloff, P. Haguenaue, H. Bartko, A. Sevin, K. Wagner, J.-L. Lizon, S. Rabien, C. Collin, G. Finger, R. Davies, D. Rouan, M. Wittkowski, K. Dodds-Eden, D. Ziegler, F. Cassaing, H. Bonnet, M. Casali, R. Genzel, and P. Lena. GRAVITY: Observing the Universe in Motion. *The Messenger*, 143:16–24, March 2011.
- [15] L. Ferrarese, P. Côté, E. Dalla Bontà, E. W. Peng, D. Merritt, A. Jordán, J. P. Blakeslee, M. Häşegan, S. Mei, S. Piatek, J. L. Tonry, and M. J. West. A Fundamental Relation between Compact Stellar Nuclei, Supermassive Black Holes, and Their Host Galaxies. *Astrophys. J.*, 644:L21–L24, June 2006.
- [16] L. Ferrarese, P. Côté, A. Jordán, E. W. Peng, J. P. Blakeslee, S. Piatek, S. Mei, D. Merritt, M. Milosavljević, J. L. Tonry, and M. J. West. The ACS Virgo Cluster Survey. VI. Isothermal Analysis and the Structure of Early-Type Galaxies. *Astrophys. J. Suppl.*, 164:334–434, June 2006.

- [17] L. Ferrarese and D. Merritt. A Fundamental Relation between Supermassive Black Holes and Their Host Galaxies. *Astrophys. J. (Lett.)*, 539:L9–L12, August 2000.
- [18] L. Ferrarese, F. C. van den Bosch, H. C. Ford, W. Jaffe, and R. W. O’Connell. *Hubble Space Telescope* photometry of the central regions of Virgo cluster elliptical galaxies. 3: Brightness profiles. *Astron. J.*, 108:1598–1609, November 1994.
- [19] J. Frank and M. J. Rees. Effects of massive central black holes on dense stellar systems. *Mon. Not. R. Astron. Soc.*, 176:633–647, September 1976.
- [20] S. Gillessen, F. Eisenhauer, S. Trippe, T. Alexander, R. Genzel, F. Martins, and T. Ott. Monitoring Stellar Orbits Around the Massive Black Hole in the Galactic Center. *Astrophys. J.*, 692:1075–1109, February 2009.
- [21] J. G. Hills. Hyper-velocity and tidal stars from binaries disrupted by a massive Galactic black hole. *Nature*, 331:687–689, February 1988.
- [22] D. Hooper and T. Linden. Origin of the gamma rays from the Galactic Center. *Phys. Rev. D*, 84(12):123005, December 2011.
- [23] C. Hopman and T. Alexander. Resonant Relaxation near a Massive Black Hole: The Stellar Distribution and Gravitational Wave Sources. *Astrophys. J.*, 645:1152–1163, July 2006.
- [24] C. Hopman and T. Alexander. The Effect of Mass Segregation on Gravitational Wave Sources near Massive Black Holes. *Astrophys. J. Letts.*, 645:L133–L136, July 2006.
- [25] A. Krabbe, R. Genzel, A. Eckart, F. Najarro, D. Lutz, M. Cameron, H. Kroker, L. E. Tacconi-Garman, N. Thatte, L. Weitzel, S. Drapatz, T. Geballe, A. Sternberg, and R. Kudritzki. The Nuclear Cluster of the Milky Way: Star Formation and Velocity Dispersion in the Central 0.5 Parsec. *Astrophys. J. Letts.*, 447:L95+, July 1995.
- [26] N. A. Krall and A. W. Trivelpiece. *Principles of plasma physics*. McGraw-Hill Kogakusha, 1973.
- [27] T. R. Lauer, E. A. Ajhar, Y.-I. Byun, A. Dressler, S. M. Faber, C. Grillmair, J. Kormendy, D. Richstone, and S. Tremaine. The Centers of Early-Type Galaxies with HST.I. An Observational Survey. *Astron. J.*, 110:2622, December 1995.
- [28] A. P. Lightman and S. L. Shapiro. The distribution and consumption rate of stars around a massive, collapsed object. *Astrophys. J.*, 211:244–262, January 1977.
- [29] J. Magorrian and S. Tremaine. Rates of tidal disruption of stars by massive central black holes. *Mon. Not. R. Astron. Soc.*, 309:447–460, October 1999.
- [30] D. Merritt. Mass Deficits, Stalling Radii, and the Merger Histories of Elliptical Galaxies. *Astrophys. J.*, 648:976–986, September 2006.
- [31] D. Merritt. Evolution of Nuclear Star Clusters. *Astrophys. J.*, 694:959–970, April 2009.
- [32] D. Merritt. The Distribution of Stars and Stellar Remnants at the Galactic Center. *Astrophys. J.*, 718:739–761, August 2010.
- [33] D. Merritt. *Dynamics and Evolution of Galactic Nuclei*. Princeton, NJ, Princeton University Press, 575 p., 2013.
- [34] D. Merritt, T. Alexander, S. Mikkola, and C. M. Will. Testing properties of the Galactic center black hole using stellar orbits. *Physical Review D*, 81(6):062002, March 2010.
- [35] D. Merritt, T. Alexander, S. Mikkola, and C. M. Will. Stellar dynamics of extreme-mass-ratio inspirals. *Physical Review D*, 84(4):044024, August 2011.
- [36] D. Merritt, S. Mikkola, and A. Szell. Long-Term Evolution of Massive Black Hole Binaries. III. Binary Evolution in Collisional Nuclei. *Astrophys. J.*, 671:53–72, December 2007.
- [37] D. Merritt and M. Y. Poon. Chaotic Loss Cones and Black Hole Fueling. *Astrophys. J.*, 606:788–798, May 2004.
- [38] D. Merritt and M. Valluri. Resonant Orbits in Triaxial Galaxies. *Astron. J.*, 118:1177–1189, September 1999.
- [39] D. Merritt and E. Vasiliev. Orbits Around Black Holes in Triaxial Nuclei. *The Astrophysical Journal*, 726:61, January 2011.
- [40] D. Merritt and E. Vasiliev. Spin evolution of supermassive black holes and galactic nuclei. *Physical Review D*, 86(10):102002, November 2012.

- [41] D. Merritt and J. Wang. Loss Cone Refilling Rates in Galactic Nuclei. *Astrophys. J.*, 621:L101–L104, March 2005.
- [42] M. Milosavljević and D. Merritt. Long-Term Evolution of Massive Black Hole Binaries. *Astrophys. J.*, 596:860–878, October 2003.
- [43] M. N. Özisik. *Heat Conduction*. New York : Wiley., 1993.
- [44] H. B. Perets and A. Gualandris. Dynamical Constraints on the Origin of the Young B-stars in the Galactic Center. *Astrophys. J.*, 719:220–228, August 2010.
- [45] H. B. Perets, A. Gualandris, G. Kubi, D. Merritt, and T. Alexander. Dynamical Evolution of the Young Stars in the Galactic Center: N-body Simulations of the S-Stars. *Astrophys. J.*, 702:884–889, September 2009.
- [46] H. B. Perets, C. Hopman, and T. Alexander. Massive Perturber-driven Interactions between Stars and a Massive Black Hole. *Astrophys. J.*, 656:709–720, February 2007.
- [47] P. C. Peters. Gravitational Radiation and the Motion of Two Point Masses. *Phys. Rev. B*, 136:1224–1232, November 1964.
- [48] M. Y. Poon and D. Merritt. A Self-Consistent Study of Triaxial Black Hole Nuclei. *Astrophys. J.*, 606:774–787, May 2004.
- [49] K. P. Rauch and S. Tremaine. Resonant relaxation in stellar systems. *New Astron.*, 1:149–170, October 1996.
- [50] M. J. Rees. ‘Dead quasars’ in nearby galaxies? *Science*, 247:817–823, February 1990.
- [51] N. Sabha, A. Eckart, D. Merritt, M. Zamaninasab, G. Witzel, M. García-Marín, B. Jalali, M. Valencia-S., S. Yazici, R. Buchholz, B. Shahzamanian, C. Rauch, M. Horrobin, and C. Straubmeier. The S-star cluster at the center of the Milky Way. On the nature of diffuse NIR emission in the inner tenth of a parsec. *Astron. Ap.*, 545:A70, September 2012.
- [52] E. E. Salpeter. The Luminosity Function and Stellar Evolution. *Astrophys. J.*, 121:161, January 1955.
- [53] N. Sambhus and S. Sridhar. Stellar Orbits in Triaxial Clusters around Black Holes in Galactic Nuclei. *Astrophys. J.*, 542:143–160, October 2000.
- [54] R. Schödel. The Milky Way Nuclear Star Cluster in Context. In M. R. Morris, Q. D. Wang, & F. Yuan, editor, *Astronomical Society of the Pacific Conference Series*, volume 439 of *Astronomical Society of the Pacific Conference Series*, page 222, May 2011.
- [55] A. Seth, M. Agüeros, D. Lee, and A. Basu-Zych. The Coincidence of Nuclear Star Clusters and Active Galactic Nuclei. *Astrophys. J.*, 678:116–130, May 2008.
- [56] S. Sigurdsson and M. J. Rees. Capture of stellar mass compact objects by massive black holes in galactic cusps. *Mon. Not. R. Astron. Soc.*, 284:318–326, January 1997.
- [57] P. F. Spinnato, M. Fellhauer, and S. F. Portegies Zwart. The efficiency of the spiral-in of a black hole to the Galactic Centre. *Mon. Not. Royal Astron. Soc.*, 344:22–32, September 2003.
- [58] L. Spitzer. *Dynamical evolution of globular clusters*. Princeton, NJ, Princeton University Press, 1987, 191 p., 1987.
- [59] D. Syer and A. Ulmer. Tidal disruption rates of stars in observed galaxies. *Mon. Not. R. Astron. Soc.*, 306:35–42, June 1999.
- [60] M. Valluri and D. Merritt. Regular and Chaotic Dynamics of Triaxial Stellar Systems. *Astrophys. J.*, 506:686–711, October 1998.
- [61] E. Vasiliev and D. Merritt. The Loss Cone Problem in Axisymmetric Nuclei. *The Astrophysical Journal*, 000:00, November 2013.
- [62] J. Wang and D. Merritt. Revised Rates of Stellar Disruption in Galactic Nuclei. *Astrophys. J.*, 600:149–161, January 2004.
- [63] C. M. Will. Capture of non-relativistic particles in eccentric orbits by a Kerr black hole. *Classical and Quantum Gravity*, 29(21):217001, November 2012.
- [64] K. Zubovas, S. Nayakshin, and S. Markoff. Sgr A* flares: tidal disruption of asteroids and planets? *Mon. Not. R. Astron. Soc.*, 421:1315–1324, April 2012.